NAVAL POSTGRADUATE SCHOOL

MONTEREY, CALIFORNIA

THESIS

EQUILIBRIUM TRANSPORT IN DOUBLE-DIFFUSIVE CONVECTION

by

D. Paul Smith

June 2011

Thesis Advisor:	Timour Radko
Second Reader:	Jason Flanagan

REPORT DOCUMENTATION PAGE	*Form Approved OMB No. 0704-0188*

1. AGENCY USE ONLY *(Leave blank)*	**2. REPORT DATE** June 2011	**3. REPORT TYPE AND DATES COVERED** Master's Thesis

4. TITLE AND SUBTITLE Equilibrium Transport in Double-Diffusive Convection	**5. FUNDING NUMBERS**
6. AUTHOR(S) D. Paul Smith	
7. PERFORMING ORGANIZATION NAME(S) AND ADDRESS(ES) Naval Postgraduate School Monterey, CA 93943-5000	**8. PERFORMING ORGANIZATION REPORT NUMBER**
9. SPONSORING /MONITORING AGENCY NAME(S) AND ADDRESS(ES) N/A	**10. SPONSORING/MONITORING AGENCY REPORT NUMBER**

11. SUPPLEMENTARY NOTES
The views expressed in this thesis are those of the author and do not reflect the official policy or position of the Department of Defense or the U.S. Government. IRB Protocol Number ____N/A______

12a. DISTRIBUTION / AVAILABILITY STATEMENT Approved for public release; distribution is unlimited	**12b. DISTRIBUTION CODE** A

13. ABSTRACT (maximum 200 words)

This study examines mixing characteristics of double-diffusive convection for a wide range of fluids. Our approach involves Direct Numerical Simulation (DNS) utilizing de-aliased pseudo-spectral method. To expedite these simulations the numerical algorithm was parallelized using Message Passing Interface (MPI) calculations in both two and three dimensions. A theoretical model of equilibrium double-diffusive transport is presented, which emphasizes the role of secondary instabilities of salt fingers in saturation of their linear growth. Theory assumes that the fully developed equilibrium state is characterized by the comparable growth rates of primary and secondary instabilities. This assumption makes it possible to formulate a simple and efficient algorithm for computing diffusivities of heat and salt as a function of the background property gradients and molecular parameters. The model predicts that the double-diffusive transport of heat and salt rapidly intensifies with decreasing density ratio. Fluxes are less sensitive to molecular characteristics, mildly increasing with Prandtl number (Pr) and decreasing with diffusivity ratio (τ). Theory is successfully tested by a series of direct numerical simulations which span a wide range of Pr and τ.

Double diffusion occurs on the micro-scale and computer technology is just now reaching the processing speeds needed to fully resolve this complex phenomenon in three dimensions. In addition to the well-known "salt fingering" within the oceans, double diffusion occurs in many other statically stable regions, both terrestrially and beyond our atmosphere. Understanding this phenomenon could prove essential as we continue to discover new worlds and new areas within our galaxy, including here on terra firma.

14. SUBJECT TERMS Salt Fingers, Double Diffusion, Double-Diffusive Convection, Heat Flux, Salt Flux, Prandtl Number, Prandtl, Diffusivity, Diffusivity Ratio, Growth Rate Balance, Salt Finger Growth Rate, Thermohaline, Diffusive Convection, Buoyancy, Ocean Circulation, Ocean Convection, Turbulent Mixing	**15. NUMBER OF PAGES** 81
	16. PRICE CODE

17. SECURITY CLASSIFICATION OF REPORT Unclassified	**18. SECURITY CLASSIFICATION OF THIS PAGE** Unclassified	**19. SECURITY CLASSIFICATION OF ABSTRACT** Unclassified	**20. LIMITATION OF ABSTRACT** UU

NSN 7540-01-280-5500

Standard Form 298 (Rev. 2-89)
Prescribed by ANSI Std. 239-18

THIS PAGE INTENTIONALLY LEFT BLANK

EQUILIBRIUM TRANSPORT IN DOUBLE-DIFFUSIVE CONVECTION

D. Paul Smith
Lieutenant, United States Navy
B.S., Old Dominion University, 2005

Submitted in partial fulfillment of the
requirements for the degree of

MASTER OF SCIENCE IN METEOROLOGY AND PHYSICAL OCEANOGRAPHY

from the

NAVAL POSTGRADUATE SCHOOL
June 2011

Author: D. Paul Smith

Approved by: Timour Radko
Thesis Advisor

Jason Flanagan
Second Reader

Jeff Paduan
Chair, Department of Oceanography

THIS PAGE INTENTIONALLY LEFT BLANK

ABSTRACT

This study examines mixing characteristics of double-diffusive convection for a wide range of fluids. Our approach involves Direct Numerical Simulation (DNS) utilizing de-aliased pseudo-spectral method. To expedite these simulations the numerical algorithm was parallelized using Message Passing Interface (MPI) calculations in both two and three dimensions. A theoretical model of equilibrium double-diffusive transport is presented, which emphasizes the role of secondary instabilities of salt fingers in saturation of their linear growth. Theory assumes that the fully developed equilibrium state is characterized by the comparable growth rates of primary and secondary instabilities. This assumption makes it possible to formulate a simple and efficient algorithm for computing diffusivities of heat and salt as a function of the background property gradients and molecular parameters. The model predicts that the double-diffusive transport of heat and salt rapidly intensifies with decreasing density ratio. Fluxes are less sensitive to molecular characteristics, mildly increasing with Prandtl number (Pr) and decreasing with diffusivity ratio (τ). Theory is successfully tested by a series of direct numerical simulations which span a wide range of Pr and τ.

Double diffusion occurs on the micro-scale and computer technology is just now reaching the processing speeds needed to fully resolve this complex phenomenon in three dimensions. In addition to the well-known "salt fingering" within the oceans, double diffusion occurs in many other statically stable regions, both terrestrially and beyond our atmosphere. Understanding this phenomenon could prove essential as we continue to discover new worlds and new areas within our galaxy, including here on terra firma.

THIS PAGE INTENTIONALLY LEFT BLANK

TABLE OF CONTENTS

LIST OF FIGURES

LIST OF TABLES

THIS PAGE INTENTIONALLY LEFT BLANK

ACKNOWLEDGMENTS

A special thanks to Dr. Timour Radko for ruining any free time I have when I just look out over the ocean. I can never just look and wonder anymore without trying to also come up with a solution. His expertise in the complex world of double-diffusive convection and his passion to better understand and model this phenomenon and its impact on larger scale circulations is immeasurable and the oceanography community benefits greatly from his dedication.

This thesis would not be possible without the use of high performance computers and an in-depth knowledge of these systems. That being said, a huge thanks to Mike Cook who has spent countless hours mentoring and teaching me the art and science of super-computing and data processing. Thank you, your hard work and dedication have been appreciated greatly.

Jason Flanagan, my second reader, has been a tremendous help in providing me with insight and know-how in organizing this thesis. Thank you.

To friends and family and the love and support of those back home, you are my biggest driving forces and I have never taken for granted where I am from and how I got to where I am today You are all the reason I do what I do and continue to make the U.S. Navy my career. I love you all!

To Arabella and Kerrigan, Daddy loves you both with all his heart. Thank you for being my great inspiration and the reason I do my best each and every day. Words cannot express how proud I am of both of you. Now go be smarter than Daddy and change the world for the better.

THIS PAGE INTENTIONALLY LEFT BLANK

I. INTRODUCTION

Double diffusion is the instability of a stratified fluid at rest whose density is determined by two components diffusing at different rates. Such a configuration can be unstable even if the density of the fluid is increasing downwards. The resulting double-diffusive convection has long been recognized as a significant, and in many cases dominant, mixing process in the ocean, where warm and salty water is often located above cold and fresh. In this case, the faster diffuser (temperature *T*) is stabilizing and the slower diffuser (salinity *S*) is destabilizing, resulting in the salt finger form of double-diffusive convection (Figure 1), which is the main focus of this discussion. Equation Section (Next)

Salt fingers are mere millimeters in diameter and can grow to a length of over 20 centimeters (Pickard 1990). Double-diffusive convection interactions were originally noted by W. S. Jevons (Jevons 1857) and were the first recorded occurrences of this phenomenon. At the time, Jevons was trying to model cirrus clouds when he inadvertently discovered double-diffusive convection within the laboratory environment. In his entry to *Edinburgh and Dublin Philosophical Magazine and Journal of Science* in 1857*,* Jevons used a warm sugar solution over a fresh water solution in a lab experiment and reported below:

> The parts of these strata, however, which are immediately in contact, soon communicate their heat and tend to assume a mean temperature; and it is evident that whenever this is the case, the portions of liquid containing sugar must always be slightly denser than those that are pure, and must consequently sink below and displace the latter.
>
> We shall thus have portions of the upper stratum continually sinking into the lower, and corresponding portions of the lower rising through the upper; and this movement, as the experiment demonstrates, takes place by an *interfiltration of minute, thread-like streams*.

The first physical model of salt fingers was developed by Dr. Melvin E. Stern (Stern 1960) more than a century later, which marks the beginning of the modern theory of double-diffusive convection. This phenomenon is better understood today due to the use of high performance computers (Radko and Stern 1999; Kimura and Smyth 2007;

Prikasky 2007; Caro 2009) important insights were brought by laboratory studies (Krishnamurti 2003) and field measurements with in the ocean (Gargett 1982). While it is still not fully understood how these minute phenomena impact larger scale circulations, it is widely believed that they may hold the key to understanding the driving forces behind the general circulation of the ocean and therefore, the Earth's climate.

In addition to oceanographic applications, compositionally driven double-diffusive convection affects heat and material transport in a variety of other geo- and astrophysical fluid systems, from magmatic melts (Tait and Jaupart 1989) to the interiors of giant planets and stars (Guillot 1999; Vauclair 2004; Charbonnel and Zahn 2007; Stancliffe et al.,, 2007).

A. SALT-FINGERS IN THE OCEAN

Salt fingers occur in nature in statically stable environments (Figures 2 and 3), where temperature and salinity perturbations diffuse at different rates causing fingers to form within a body of water. Salt fingers are common in the main thermocline, where water tends to be warmer and saltier near the sea-surface due to a combination of surface evaporation and heating. Individual parcels displaced downward lose their thermal properties faster than salinity, causing them to be denser than the surrounding fluid (Figure 1) and continue to sink. This causes the parcel to continue descending (Stern 1960; Schmitt et al.,, 2005), which results in vigorous double-diffusive convection discussed in this study.

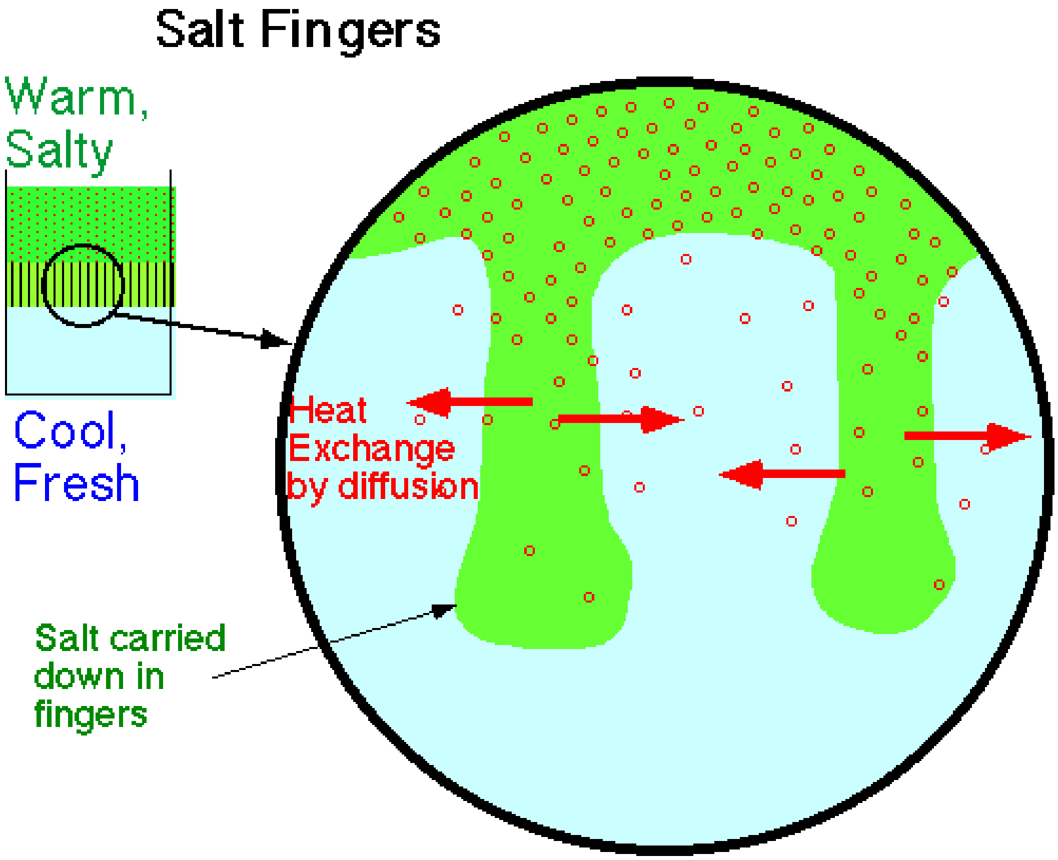

Figure 1. Schematic diagram illustrating the physical mechanisms of double-diffusive convection.

An example of this process can be found at the output of the Mediterranean through the Straits of Gibraltar. The outflow from the Mediterranean Sea is much saltier and warmer than the Atlantic Ocean water at depth (approximately 2400 meters) causing double-diffusive interactions deep underneath the surface of the ocean.

It is also believed that salt fingers contribute to the ocean's large scale mixing and could be important to climate models (Gargett and Schmitt 1982). Today's climate models cannot resolve such minute scales within a reasonable forecast time, so finding physical parameterizations that can be fed into these models can greatly improve their accuracy. Understanding the impact of these processes on large scale circulations can also help to provide better ice melt forecasts, as well as higher resolution global and regional oceanographic forecast models across all spectrums within oceanography.

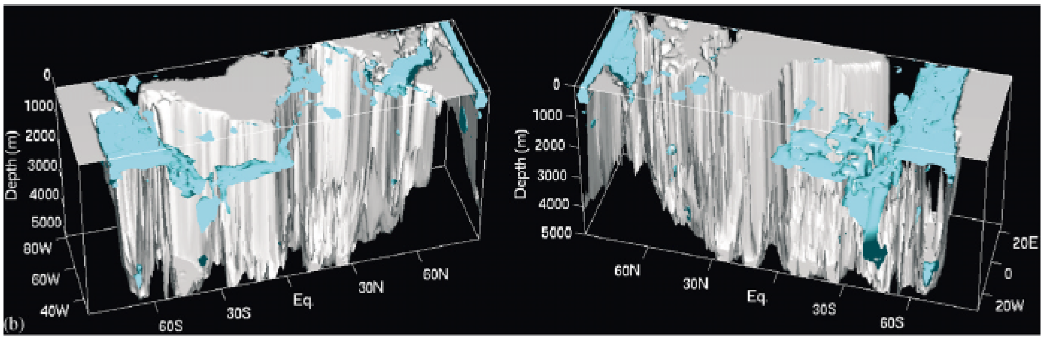

Figure 2. Diagram illustrating the geographic distribution of diffusive-convection, which occurs in approximately 15% of the world’s oceans. Unlike salt fingering, this phenomenon occurs when cold fresh water is located above warm and salty.

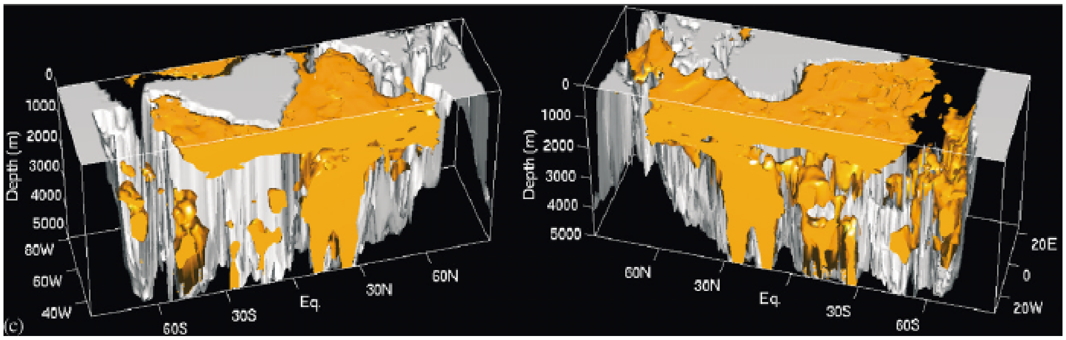

Figure 3. Diagram illustrating geographic locations of salt fingers, which occurs in approximately 30% of the world’s oceans.

B. BEYOND OCEANOGRAPHY

By extending our knowledge of oceanographic double-diffusion and changing background parameters we can get a “feel” of how double diffusive convection changes in other environments.

External planetary systems, such as the atmospheric makeup of planets within our solar system, are represented by a much lower Prandtl number (Pr) than in our oceans, ($Pr = 10^{-5}$ verses $Pr = 7$). Estimates show that for Jupiter’s atmosphere (radiation driven), $Pr \approx 10^{-4}$ and for the metallic interior (conduction driven), $Pr \approx 10^{-2}$ (Bagenal et al.,, 2004). Decreasing Pr from the oceanographic value of 7, allows us to build a better understanding of how double diffusive convection behaves within these foreign bodies.

The interior temperature and Helium within our own sun and other stars is also a natural area where double diffusive convection occurs as interior temperature and Helium diffuse at separate rates. Metallic fingers are theorized in these systems to consist of metallic “blobs” that descend similar to the oceanographic warmer denser fluid, with heat diffusing much quicker than the heavy metal composition within the fluid (Vauclair 2003). Another manifestation of active salt fingering in nature, the high Prandtl number within magma flows, has close similarities to oceanographic salt fingers (Tait 1989).

Sugar-salt interactions have been modeled in the laboratory environment starting with Jevons in 1857 with pure water and, hydrochloric acid and white sugar (Jevons 1857). The sugar-salt solution is different to prior cases, in both the Prandtl number and the diffusivity ratio. However, we include this case so as to achieve a more complete understanding.

While many regimes are currently beyond the modeling capabilities of even for the most powerful super computers, in this study we strive to gain a quantitative understanding within the accessible limits of Pr, τ, and R_ρ values. Many regimes we wish to explore are outside this reach and we are pushing the limits of what is possible with today’s computer processing speeds.

C. EXTANT MODELS OF EQUILIBRIUM TRANSPORT

A fundamental question in double-diffusive convection theory concerns the equilibrium transport of temperature, salinity, chemical tracers, and momentum. The quantification of double-diffusive fluxes and their dependencies on the background temperature and salinity gradients—so-called flux-gradient laws—is an essential step in linking the microstructure dynamics with larger scales of motion. This problem has motivated numerous laboratory (Lambert and Demenkow 1972; Griffiths and Ruddick 1980) and field (Schmitt et al.,, 1987; Schmitt et al.,, 2005) experiments, as well as theoretical (Stern 1969; Kunze 1987) and numerical (Shen 1995; Stern et al.,, 2001; Kimura and Smyth 2007, 2011; Traxler et al.,, 2011; Stellmach et al.,, 2011) models.

While the linear stability theory of double diffusion (Stern 1960; Baines and Gill 1969) is well developed and fully understood, it does not explain the saturation of primary double-diffusive instabilities—the problem of equilibrium double-diffusive transport is complicated and principally nonlinear.

Numerous attempts have been made to deduce flux-gradient laws from first principles. The first and perhaps the most influential idea was introduced by Stern (1969), who suggested that the linear growth of salt fingers is arrested when the Stern number

$$A = \frac{\alpha F_{T\dim} - \beta F_{S\dim}}{\nu(\alpha \overline{T}_z - \beta \overline{S}_z)}$$

reaches O(1). F_{Tdim} and F_{Sdim} here are the dimensional temperature and salinity fluxes; $\overline{T}_z$ and $\overline{S}_z$ are the vertical gradients; α, β are the thermal expansion and haline contraction coefficients respectively; ν is the molecular viscosity. Stern's physical argument is compelling. When A exceeds unity, the unbounded salt finger system becomes unstable with respect to collective instability, a term used to describe the spontaneous excitation of gravity waves by salt fingers. Stern suggested that collective instability could disrupt salt fingers, thereby arresting the development of primary instabilities.

At first glance, various pieces of indirect evidence seemed to validate Stern's hypothesis. Oceanographic measurements (Hebert 1988; Innoue et al.,, 2008) tend to produce O(1) values of A. Kunze (1987) gave an alternative argument in support of the Stern number constraint. He showed that $A = 1$ is equivalent to the Richardson number (Ri) of ¼ based on scales of individual salt fingers. Kunze suggested that the well-known criterion for the instability of horizontal, inviscid and nondiffusive parallel flows (Richardson 1920; Howard 1961; Miles 1961), i.e. Ri < ¼, can be extended to viscous, diffusive and vertically oriented fingers.

However, closer inspection has revealed certain inconsistencies in the Stern-Kunze hypothesis. For instance, in many laboratory experiments, salt and sugar replace heat and salt as buoyancy components (Stern and Turner 1969; Lambert and Demenkow 1972; Griffiths and Ruddick 1980; Taylor and Veronis 1996; Krishnamurti 2003).

Typical values of Stern number in this case are extremely low. Lambert and Demenkow (1972) report Stern numbers as low as $A = 2 \cdot 10^{-3}$, casting some doubt on the generality of the Stern number constraint. On the theoretical side, a critical advance was made by Holyer (1984), who performed a formal linear stability analysis for vertical steady salt fingers. She discovered direct, relatively small-scale — comparable to the salt finger width — secondary instabilities, which typically grow much faster than the collective instability modes. Unlike collective instabilities, Holyer modes grow regardless of the (finite) amplitude of salt fingers and thus regardless of the specific values of A. Numerical simulations (Shen 1995; Radko and Stern 1999) confirmed Holyer's ideas by demonstrating that the equilibration of salt fingers occurs by means of the nonlinear interaction of primary instabilities with Holyer modes. Furthermore, the eddy diffusivities of heat and salt from simulations (Stern et al.,, 2001) and available observations (St. Laurent and Schmitt 1999) monotonically decrease with the density ratio, whereas the opposite trend was expected based on the Stern-Kunze constraint. The most recent and well-resolved simulations of the heat-salt system (Traxler et al.,, 2011) indicate that as the density ratio increases from 1.2 to 10, the Stern number in the equilibrium flow reduces by more than two orders of magnitude, from $A = 76$ to $A = 0.6$.

Concerns with regard to the Stern number constraint have motivated the development of alternative models for the equilibrium transport. While the general analytical description of double-diffusive transport is still lacking, several cases have already been successfully treated. Weakly nonlinear instability theory describes salt finger patterns, dynamics, and transport characteristics for the parameters near the point of marginal instability (Proctor and Holyer 1986; Radko and Stern 1999, 2000; Stern and Simeonov 2004; Radko 2010). Promising attempts to formulate physically based parameterizations of salt finger transport include the mixing length model (Stern and Simeonov 2005), a double-diffusive version of the upper bound theory (Balmforth et al., 2006), a second-order closure approach (Canuto et al., 2008), and various phenomenological models (Shen 1995; Merryfield and Grinder 1999; Radko 2008). We propose what appears to be, to date, the most general algorithm for estimating the equilibrium salt finger transport. The model is based on the properties of secondary salt finger instabilities and can be applied to a variety of parameter regimes, including small, moderate, and large Prandtl numbers, and a wide range of diffusivity ratios.

D. OUR APPROACH

Our story is a new variation on an old theme—a theme that appears, explicitly or implicitly, in almost all theories of equilibrium double-diffusive convection (Stern 1969; Holyer 1984; Kunze 1987; Stern and Simeonov 2005; Radko 2010). We revisit the idea of a competition between linear mechanisms involved in the growth of salt fingers and the disruptive action of their secondary instabilities. At the same time, we strive to avoid some debatable assumptions of earlier models, such as the link between secondary instabilities and Stern number. The competition between primary and secondary instabilities is concisely phrased in the growth rate balance assumption:

$$\lambda_2 = C\lambda_1, \tag{1}$$

where λ_1 is the typical growth rate of linear salt fingers, λ_2 is the growth rate of their secondary instabilities, and C is a dimensionless order one quantity that can be calibrated on the basis of simulations or experiments. The primary growth rate λ_1 is determined by the background gradients of temperature and salinity and by molecular characteristics (diffusivities and viscosity). The secondary instability λ_2 is also affected by these quantities, but, additionally, it depends very strongly on the amplitude of primary salt fingers. Thus, for any given background parameters and a value of C, the growth rate balance Equation (1) implicitly determines the equilibrium amplitude of salt fingers.

The physical reasoning behind Equation (1) is straightforward. As initially weak salt fingers, emerging from random small scale perturbations, grow in time, they start to develop secondary (Holyer 1984) instabilities. Unlike the primary ones, the growth rate of secondary instabilities monotonically increases with the amplitude of fingers. At first, the growth of secondary instabilities is too slow to inflict any significant damage on growing primary modes—the evolution of small amplitude fingers is adequately captured by the linear theory. However, at some point, the growth rate of secondary instabilities exceeds the primary growth rates. As a result, the secondary instabilities start to gain in magnitude, rapidly reaching the level of primary modes. Their interaction nonlinearly suppresses the growth of salt fingers. At this stage, the system reaches statistical equilibrium.

In this study, condition Equation (1) is used as the basis for a simple algorithm to determine the equilibrium amplitude of salt fingers. The growth of primary modes (λ_1) is evaluated from the linear instability theory (Stern 1960; Baines and Gill 1969). For any given amplitude of salt fingers, the growth rate of secondary instabilities (λ_2) can be computed using elements of the Floquet theory as in Holyer (1984). The amplitude of fingers is iteratively adjusted until λ_1 and λ_2 satisfies the growth rate balance Equation (1) . The model predictions are then conveniently expressed in terms of the equilibrium eddy fluxes of heat and salt.

The use of DNS has been essential to the success of our research. DNS allows us to (i) calibrate our theoretical model, (ii) validate our reference base on the growth rate balance Equation (1), and (iii) expand the sensitivity of our solutions to the background parameters. From crude calculations of man-hours spent on this project it would take 91+ years (over 800,000 hrs) to run these calculations on a single computer processor continuously. Many of these experiments are run on multiple parallel processors, sometimes 128 working simultaneously and still taking longer than a week to complete. As computing power increases, this processing time will decrease and more robust calculations and data can be collected.

This thesis is organized as follows. In Chapter II, we present DNS, focusing our inquiry on the equilibration of primary instability. A theoretical model of equilibration is presented in Chapter III. We compute the temperature and salinity fluxes as a function of density ratio for the oceanographic case ($Pr=7$, $\tau=0.01$) and successfully test (Chapter IV) the theoretical prediction by DNS. In Chapter V, we also explore a broader parameter range, including the low Prandtl number regime, relevant for astrophysical applications, and high Prandtl numbers, relevant for magmatic melts. Each case is compared with the corresponding DNS. We summarize and draw conclusions in Chapters VI while discussing future possibilities in Chapter VII.

THIS PAGE INTENTIONALLY LEFT BLANK

II. PRELIMINARY CALCULATIONS

The simplest and most direct approach to the analysis of equilibrium of salt fingering involves Direct Numerical Simulation (DNS). We used a de-aliased pseudo-spectral method described and first used for two-dimensional (Stern and Radko 1998) and three dimensional salt-fingering simulations (Radko and Stern 1999). In order to expedite the simulations the numerical algorithm was parallelized using a Message Passing Interface (MPI) algorithm in both two and three dimensions. Two dimensional model runs were performed on Anastasia, a high-performance computer cluster at Naval Postgraduate School (NPS). Three dimensional model runs were performed on the shared high-performance computer cluster Hamming, also at NPS, and Einstein, a U.S. Navy Cray XT5 high-performance computer cluster. The resources utilized, varied from 4 processors on Anastasia up to 128 simultaneous processors on Einstein for the most highly resolved cases in heat salt throughout R_ρ values of 1.1, 1.3, …, 2.9 (Tables 2 through 6). We resolve a total of ten fingers; 5 warmer, more dense and 5 cooler, less dense. However, in order to resolve the salt finger scale, these runs required anywhere from 3 days to 4 weeks to complete. With increased computing power, this time limitation to process data will decrease in future years. In turn, this will allow future graduate students the flexibility to run more data sets over longer periods and thereby address even more challenging problems in double-diffusive convection.

Following Radko and Stern (1999), we separate the temperature and salinity fields into the basic state $\left(\overline{T},\overline{S}\right)$, representing a uniform vertical gradient, and a departure $\left(T,S\right)$ from it. The two-dimensional Boussinesq equations of motion are expressed in terms of T,S and nondimensionalized using $l=\left(\frac{k_T\nu}{g\alpha\overline{T}_z}\right)^{\frac{1}{4}}$, $\frac{k_T}{l}$, $\frac{l^2}{k_T}$, and $\frac{\rho_0\nu k_T}{l^2}$ as the scales of length, velocity, time and pressure respectively. Here, (k_T,k_S) denote the molecular diffusivities of heat and salt and ρ_0 is the reference density used in the

Boussinesq approximation. The expansion/contraction coefficients are incorporated in (T,S) and $\alpha \overline{T}_z l$ is used as the scale for both temperature and salinity perturbations, resulting in

$$\begin{cases} \dfrac{\partial T}{\partial t} + \vec{\mathrm{v}} \cdot \nabla T + w = \nabla^2 T \\ \dfrac{\partial S}{\partial t} + \vec{\mathrm{v}} \cdot \nabla S + \dfrac{w}{R_\rho} = \tau \nabla^2 S \\ \dfrac{1}{\mathrm{Pr}} \left(\dfrac{\partial}{\partial t} \vec{\mathrm{v}} + \vec{\mathrm{v}} \cdot \nabla \vec{\mathrm{v}} \right) = -\nabla p + (T - S)\vec{k} + \nabla^2 \vec{\mathrm{v}} \\ \nabla \cdot \vec{\mathrm{v}} = 0, \end{cases} \tag{2}$$

where $\vec{\mathrm{v}} = (u, v, w)$ is the velocity vector. This system is unstable with respect to salt fingering (Stern 1960) for

$$1 < R_\rho < 1/\tau \,. \tag{3}$$

The key nondimensional numbers governing the evolution of system Equation (2) are the Prandtl number $\mathrm{Pr} = \dfrac{\nu}{k_T}$, the diffusivity ratio $\tau = \dfrac{k_S}{k_T}$, and the background density ratio $R_\rho = \dfrac{\alpha \overline{T}_z}{\beta \overline{S}_z}$. We also assume that, in the absence of large-scale structures, fluxes are independent of the nondimensional parameters related to the domain size (e.g., the Rayleigh number). The local flux-gradient laws are commonly used to parameterize the effects of salt fingering on the oceanic circulation and successful attempts have been made to validate the concept of an unbounded *T-S* gradient in numerical simulations (Radko and Stern 1999).

To gain a preliminary understanding of the mechanics of equilibration (R_ρ,Pr,τ), Equation (2) was solved numerically. We assume triply periodic boundary conditions for *T*, *S*, *p*, and $\vec{\mathrm{v}}$ and integrate the governing equations using a de-aliased pseudo-spectral method described in Radko and Stern (1999). In the following calculation, we use parameters relevant in the oceanographic (heat/salt) context: τ=0.01 and Pr=7. The overall density ratio is R_ρ=1.9, which is representative of the main Atlantic thermocline. The size of the computational domain (L_x = 38.2, L_y = 38.2, L_z = 76.3) is equivalent to

(5x5x10) linearly fastest growing finger wavelengths (*d*). The flow was resolved by a uniform mesh with (N_x x N_y x N_z) = (256 x 256 x 512) elements, and the model was initialized from rest by a small-amplitude random computer-generated initial (*T,S*) distribution. After a few characteristic growth periods, active statistically steady double-diffusive convection was established. Figure 4a shows a typical instantaneous (*t*=20) temperature field in the initial stage of linear growth.

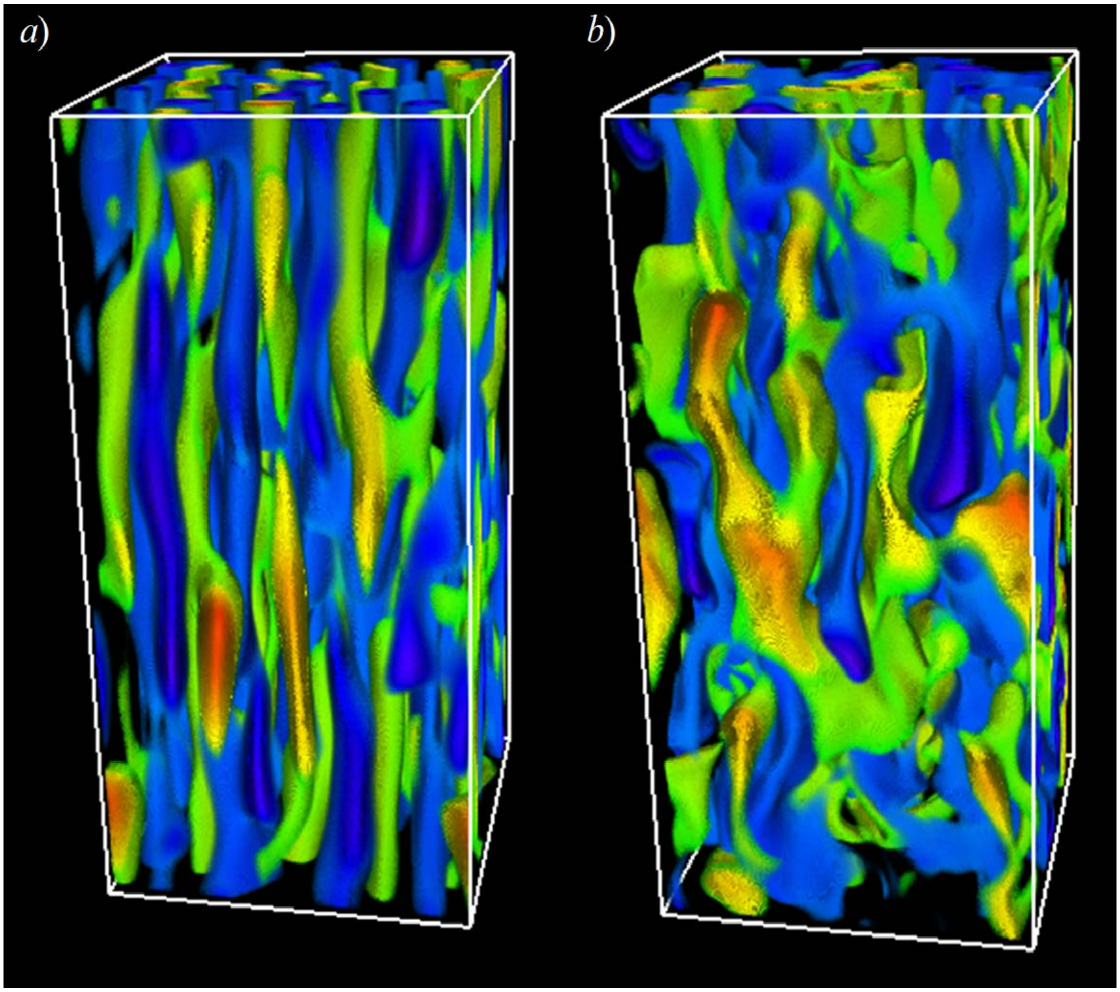

Figure 4. Equilibration of salt fingers in the numerical experiment with Pr=7, $\tau = 0.01$, $R_\rho = 1.9$. Three-dimensional instantaneous temperature fields are shown for *a*) the early stage of linear growth at *t*=20 and *b*) the fully equilibrated state at *t*=50. Red/green color corresponds to high values of *T* and low values are shown in blue.

As expected from the linear stability theory, the most rapidly growing perturbations take the form of the vertically uniform salt fingers known as elevator modes. Figure 4b presents the fully developed equilibrium regime (*t*=50). While the previously dominant elevator mode is still visible, it is now comparable in magnitude to the secondary instabilities, which act to twist the vertical fingers, adversely affecting their growth. This stage is characterized by the irregular transient patterns in the temperature field—a dramatic consequence of the nonlinear interaction between the elevator modes and their secondary instabilities.

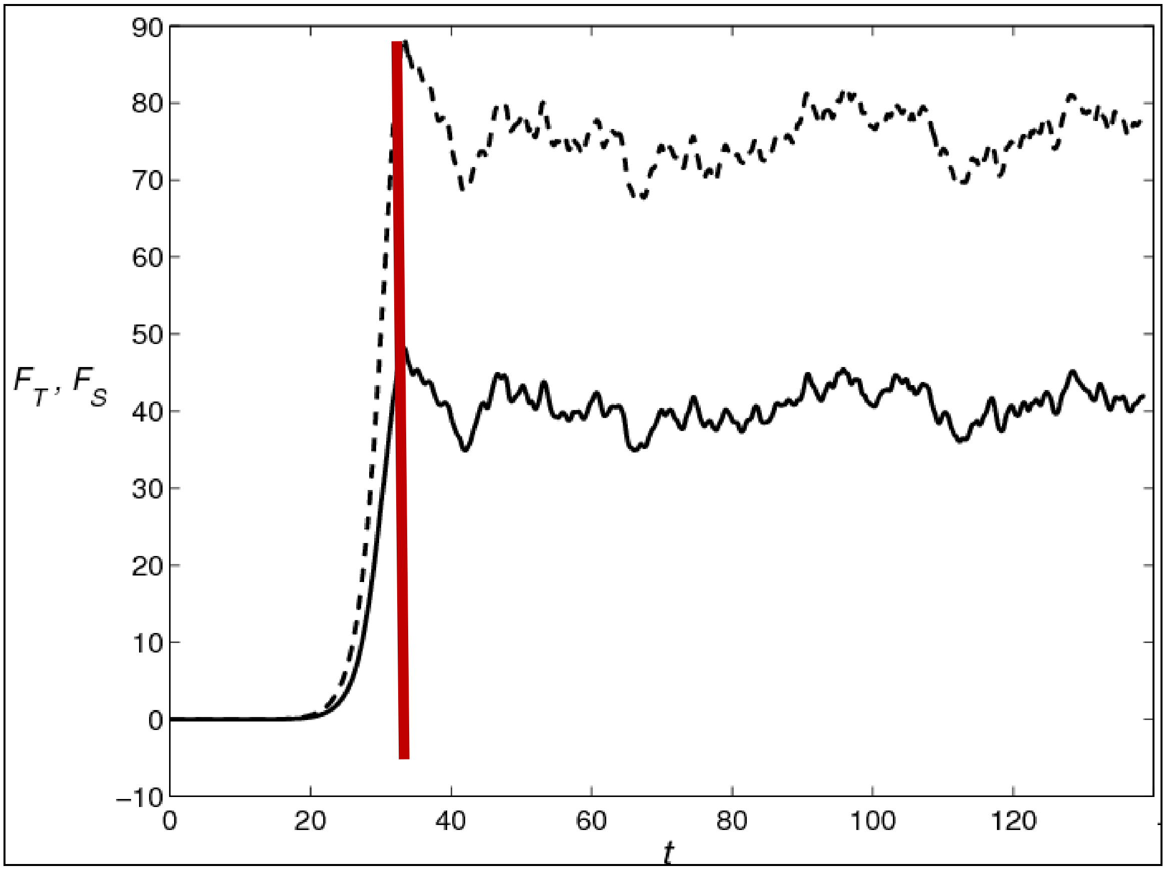

Figure 5. Time record of the temperature (solid curve) and salinity (dashed curve) fluxes for the calculation in Fig 4. Equilibrium point is marked by red line.

The transition to the statistically steady regime is illustrated in Figure 5, which shows the evolution of the spatially averaged downward temperature and salinity fluxes $(F_T, F_S) = (-\overline{wT}, -\overline{wS})$ – the sign convention is dictated by considerations of convenience.

Note that the heat flux in our system of nondimensionalization is $F_T = Nu - 1$, where Nu is the Nusselt number—the ratio of the total heat flux to the (much weaker) molecular diffusive flux. The initial stage of the simulation (t<30) is characterized by the exponential growth of fluxes, which is followed by their equilibration. After equilibration, the intensity of salt fingering remains statistically steady.

The nondimensional fluxes (F_T, F_S) can be converted to the dimensional eddy diffusivities of heat and salt $(K_{T\dim}, K_{S\dim})$ using

$$K_{T\dim} = F_T k_T, \quad K_{S\dim} = F_S k_T R_\rho. \tag{4}$$

The time mean *T-S* fluxes, averaged over the second half of the experiment in Figure 5, are $F_T = 40.88$, $F_S = 75.88$, which corresponds to the dimensional diffusivities of heat and salt of

$$K_{T\dim} = 5.6 \cdot 10^{-6} m^2 s^{-1}, \quad K_{S\dim} = 2.0 \cdot 10^{-5} m^2 s^{-1} \tag{5}$$

These values are broadly consistent with the observational estimates (St. Laurent and Schmitt, 1999) for the density ratio of $R_\rho = 1.9$.

In Figure 6, we plot typical horizontal (top panel) and vertical (lower panels) sections of temperature (left) and salinity (right) for the fully developed equilibrium regime. Temperature and salinity patterns are correlated and both reveal vertically elongated—but far from uniform—horizontally isotropic salt fingers. Salinity sections are characterized by very fine, relative to temperature, spatial scales, which is a direct consequence of the low diffusivity ratio.

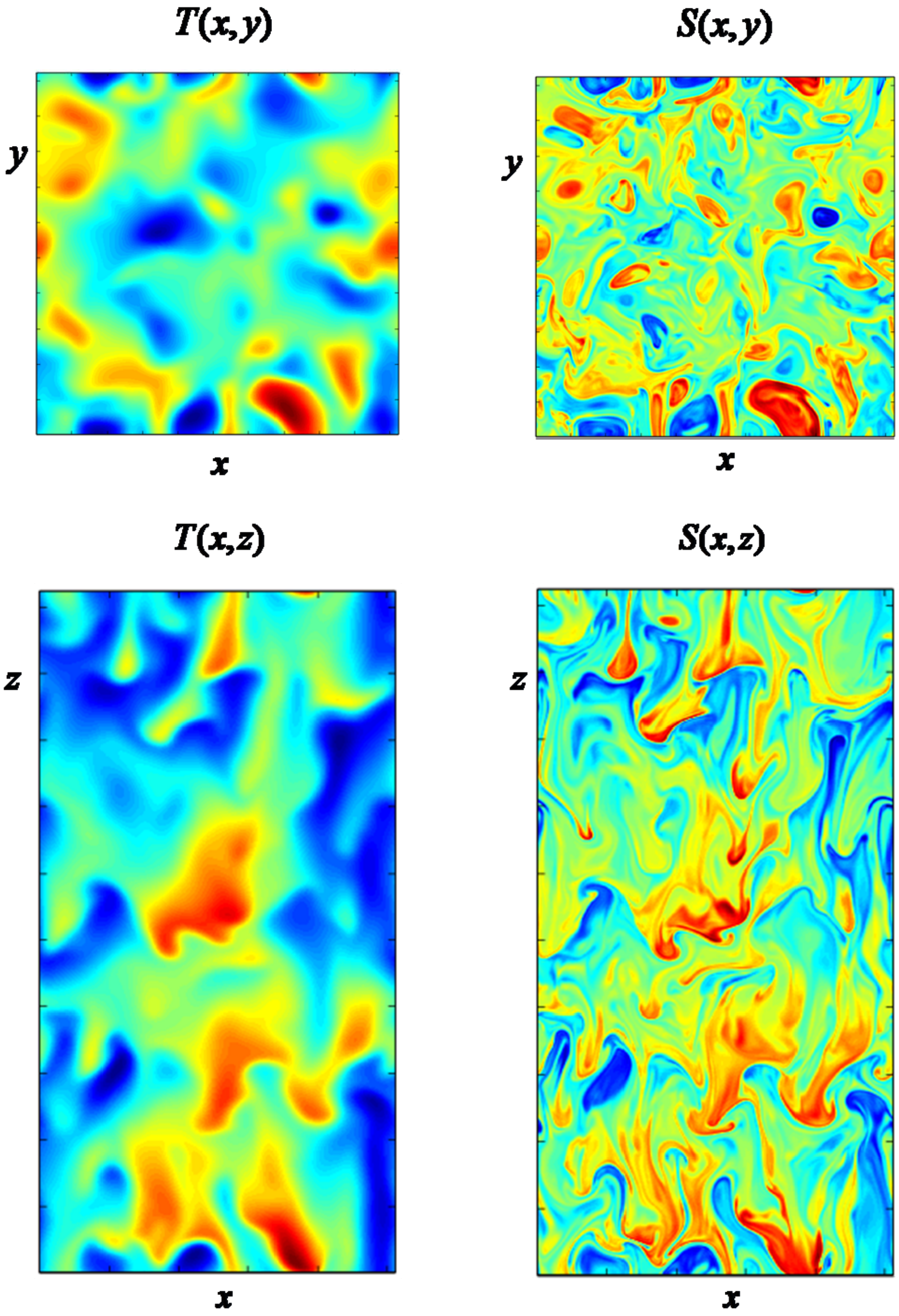

Figure 6. Horizontal (upper panels) and vertical (lower panels) sections of temperature (left) and salinity (right) for a typical fully equilibrated state of the calculation in Fig 5.

III. THEORETICAL MODEL

Guided by physical reasoning (Section D of Chapter I) and by direct numerical simulations (e.g., Chapter II), we now attempt to predict the equilibrium level of salt fingers from the growth rate balance Equation (1). The growth rate equation for the primary salt finger instabilities (Stern 1960) in our nondimensional units reduces to

$$\lambda^3 + [1+\tau+\Pr]k^2\lambda^2 + \left[(\tau+\Pr+\tau\Pr)k^4 + \Pr\left(1-R_\rho^{-1}\right)\right]\lambda + \tau\Pr k^6 - \Pr k^2\left(R_\rho^{-1}-\tau\right) = 0, \tag{6}$$

where *k* is the horizontal wavenumber of the vertically uniform elevator modes. For our purpose it is not necessary to consider inclined salt fingers since the largest growth rates are attained by the vertically oriented elevator modes (e.g., Baines and Gill 1969). For each (R_ρ,Pr,τ), we compute the largest growth rate (λ_1) by maximizing the solutions of Equation (6) with respect to *k* as in Schmitt (1979, 1983). Thus, λ_1 is uniquely determined by the governing parameters:

$$\lambda_1 = \lambda_1(R_\rho, \Pr, \tau)\,. \tag{7}$$

While the maximal growth rates of primary instabilities are identical in two (x,z) and three (x,y,z) dimensions, the secondary instabilities differ substantially. Therefore, the algorithms for computing λ_2 in two and three dimensions will be discussed separately.

A. TWO-DIMENSIONAL FORMULATION

In two dimensions, the governing equations are conveniently written in terms of the streamfunction ψ , such that $(u,w)=\left(-\frac{\partial\psi}{\partial z},\frac{\partial\psi}{\partial x}\right)$, resulting in

$$\begin{cases} \dfrac{\partial T}{\partial t} + J(\psi,T) + \dfrac{\partial\psi}{\partial x} = \nabla^2 T \\ \dfrac{\partial S}{\partial t} + J(\psi,S) + \dfrac{1}{R_\rho}\dfrac{\partial\psi}{\partial x} = \tau\nabla^2 S \\ \dfrac{\partial}{\partial t}\nabla^2\psi + J(\psi,\nabla^2\psi) = \Pr\left[\dfrac{\partial}{\partial x}(T-S) + \nabla^4\psi\right]. \end{cases} \tag{8}$$

Our next step is to use Equation (8) to examine the stability of the basic state representing the elevator modes:

$$\begin{cases} \overline{T} = A_T \sin(kx) \\ \overline{S} = A_S \sin(kx) \\ \overline{\psi} = A_\psi \cos(kx) \end{cases} \tag{9}$$

It should be mentioned that the secondary stability problem can be formulated in different ways. Holyer (1984) has chosen the wavenumber k in Equation (9) to correspond to the solution with zero primary growth rate (k_o). This restriction defines a well-posed stability problem with the regular basic steady state. There is only one reason to question this formulation. It is apparent from DNS (Stern et al.,, 2001; Traxler et al.,, 2011) and even indicated by some oceanographic field measurements (Gargett and Schmitt, 1982) that the horizontal wavenumber of dominant fully developed salt fingers is more accurately approximated by k_{max}, the wavenumber corresponding to the maximum growth rate, than by k_o. Use of $k=k_{max}$ in Equation (9); however, results in the time-dependent basic state, and therefore the conventional methods of stability analysis cannot be applied directly. This problem is not uncommon and not insurmountable. Notable examples of analyzing such flows come from studies based on the Kolmogorov model—the sinusoidal parallel flow in viscous fluid (Sivashinsky 1985; Manfroy and Young, 1999 2002; Balmforth and Young 2002, 2005). Since the unforced viscous parallel flow would inevitably decay, the Kolmogorov model circumvents this problem by introducing artificial forcing in the momentum equation that maintains the steady state. Variations on the same principle, often referred to as the quasi steady state approximation or a "frozen flow" method, have been successfully applied to numerous stability problems (e.g., Lick 1964; Robinson 1976) including salt fingers (Kimura and Smyth 2011).

A choice has to be made at this point between the approach of a purist, insisting on formal mathematical consistency, and that of a practically-oriented researcher, more concerned by the consistency with patterns realized in nature. We have examined both models, $k=k_0$ and $k=k_{max}$, and the results are qualitatively similar. The prediction of the $k=k_{max}$ model is closer to the corresponding DNS, and therefore we limit the following discussion to the configuration based on the fastest growing solution. We assume that in the regime close to equilibrium the amplitude Equation (9) is maintained at a quasi-steady level for k=k$_{max}$ and separate the solution into the dominant basic state and small perturbation:

$$\left(T,S,\psi\right)=\left(\overline{T},\overline{S},\overline{\psi}\right)+\left(T',S',\psi'\right). \tag{10}$$

Equation (8) is linearized as follows:

$$\begin{cases}\dfrac{\partial T'}{\partial t}-A_\psi k\sin(kx)\dfrac{\partial T'}{\partial z}-A_T k\cos(kx)\dfrac{\partial\psi'}{\partial z}+\dfrac{\partial\psi'}{\partial x}=\nabla^2 T'\\ \dfrac{\partial S'}{\partial t}-A_\psi k\sin(kx)\dfrac{\partial S'}{\partial z}-A_S k\cos(kx)\dfrac{\partial\psi'}{\partial z}+\dfrac{1}{R_\rho}\dfrac{\partial\psi'}{\partial x}=\tau\nabla^2 S'\\ \dfrac{\partial}{\partial t}\nabla^2\psi'-A_\psi k\sin(kx)\dfrac{\partial\nabla^2\psi'}{\partial z}-A_\psi k^3\sin(kx)\dfrac{\partial\psi'}{\partial z}=\Pr\left[\dfrac{\partial}{\partial x}(T'-S')+\nabla^4\psi'\right].\end{cases} \tag{11}$$

To examine the stability properties of the linear system Equation (11), we use the Floquet technique in which the perturbation is sought in the following form:

$$\begin{pmatrix}T'\\ S'\\ \psi'\end{pmatrix}=\exp(ifkx+imz+\lambda t)\sum_{n=-N}^{N}\begin{pmatrix}T_n\\ S_n\\ \psi_n\end{pmatrix}\exp(inkx), \tag{12}$$

where λ is the growth rate, *m* is the vertical wavenumber, and *f* is the Floquet coefficient, which controls the fundamental wavelength in *x*. Substituting Equation (12) into the linear system Equation (11) and collecting the individual Fourier components allows us to express the governing equations in the matrix form:

$$\lambda\vec{\xi}=\boldsymbol{A}\vec{\xi}, \tag{13}$$

where

$$\vec{\xi}=(T_{-N},S_{-N},\psi_{-N},T_{-N+1},S_{-N+1},\psi_{-N+1},\ \ldots\ ,T_N,S_N,\psi_N), \tag{14}$$

and $\boldsymbol{A}$ is the square matrix whose elements are functions of$\left(k,m,f,R_\rho,\Pr,\tau,N,A_T,A_S,A_\psi\right)$.

The growth rates of the normal modes of the linear system Equation (11) correspond to the eigenvalues of $\boldsymbol{A}$. For each set of governing parameters, we determine the eigenvalue with the maximum real part, which represents the fastest growing mode.

The value of this growth rate is then maximized with respect to m and f. Note that the symmetry and periodicity properties of our system are such that the Floquet coefficient f needs to be varied only within the range $0 \le f \le 0.5$.

The coefficients (A_T,A_S,A_ψ) of the normal mode Equation (9) are connected, for k=k$_{max}$, by the following relations:

$$\begin{cases} A_T\left(\lambda_1 + k_{\max}^2\right) = k_{\max} A_\psi \\ A_S\left(\lambda_1 + \tau k_{\max}^2\right) = \dfrac{k_{\max}}{R_\rho} A_\psi, \end{cases} \tag{15}$$

and therefore the amplitude vector (A_T,A_S,A_ψ) can be immediately determined from any component—for instance from the temperature amplitude (A_T). As described below, the solution rapidly converges with increasing resolution ($N \to \infty$). Thus, the fastest growing secondary instability is determined by four parameters:

$$\lambda_2 = \lambda_2(R_\rho, \Pr, \tau, A_T). \tag{16}$$

Our next step is to solve the growth rate balance Equation (1). For each set of governing parameters (R_ρ,Pr,τ), we determine the primary growth rate λ_1 using Equation (6). Suppose now that the value of C in Equation (1) is known. Then, by varying the amplitude of the normal mode A_T we can readjust Equation (16) until the growth rate balance is satisfied. The dependence $\lambda_2(A_T)$ takes the form of a monotonically increasing, nearly linear relation. For $A_T = 0$, the secondary instability problem becomes identical to that of primary instability and therefore $\lambda_2 = \lambda_1$. A corollary of this observation is that solutions of Equation (1) exist only for $C>1$, as indicated by the schematic in Figure 7.

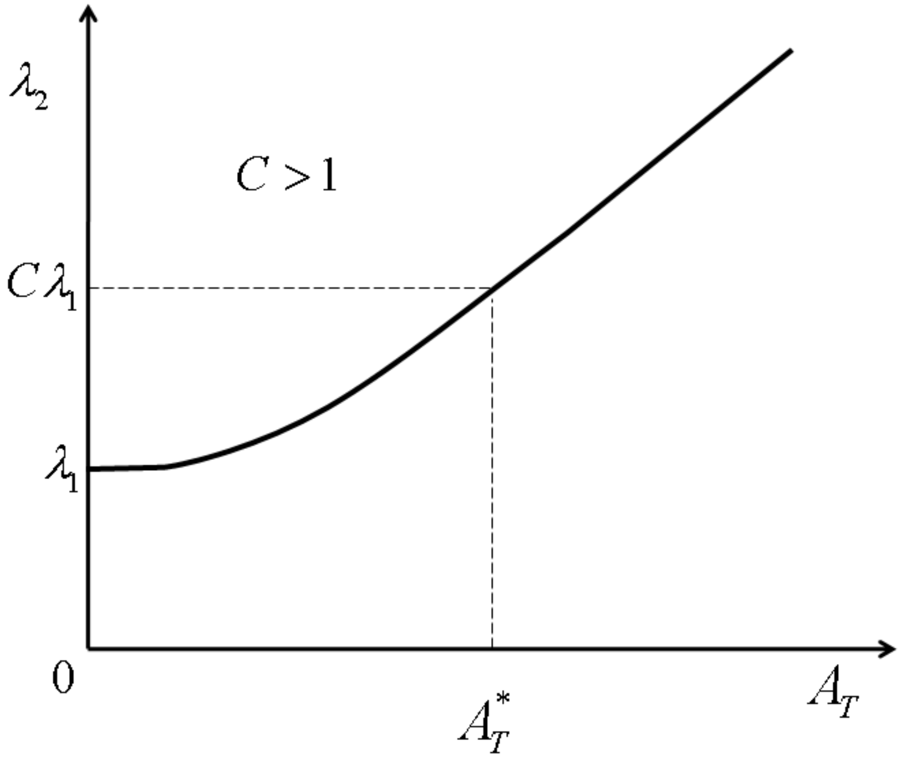

Figure 7. Illustration of the algorithm for predicting the equilibrium amplitude of salt fingers. The growth rate of the secondary instability (λ_2) monotonically increases with the amplitude of salt fingers (A_T). We hypothesize that the equilibrium (A_T^*) is reached when $\lambda_2 = C\,\lambda_1$.

An iterative procedure for solving the growth rate balance Equation (1) was coded in MAPLE and it typically required 7–8 iterations for the model to converge, within a negligible relative error of 10^{-5}, to the sought-after solution $A_T = A_T^*$. The vertical fluxes are then reconstructed using Equation (9) and Equation (15) as follows:

$$\begin{cases} F_T = \overline{wT} = \dfrac{1}{2} A_T^2 \left(\lambda_1 + k_{\max}^2\right) \\ F_S = \overline{wS} = \dfrac{1}{2R_\rho} A_T^2 \dfrac{\left(\lambda_1 + k_{\max}^2\right)^2}{\left(\lambda_1 + \tau k_{\max}^2\right)}. \end{cases} \tag{17}$$

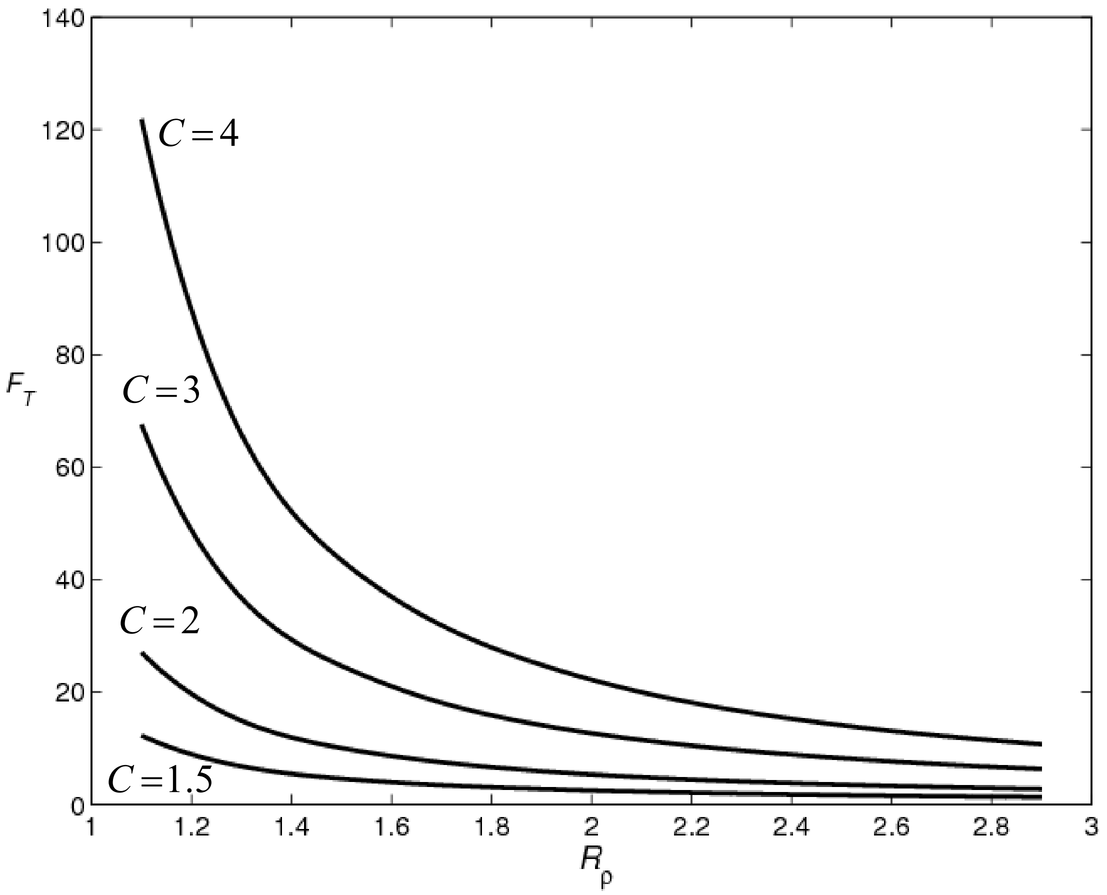

Figure 8. Heat flux in the theoretical two-dimensional model for various values of *C*.

In Figure 8, the predicted heat and salt (Pr=7, τ=0.01) fluxes are plotted as a function of density ratio (R_ρ) for various values of *C*. Fluxes increase with *C* and rapidly reduce with R_ρ. The calculations in Figure 8 were performed for *N*=32. However, the specific number of Fourier harmonics involved in the Floquet calculation is not particularly important. The rapid convergence of the solution with increasing *N* is indicated in Table 1. The very crude truncation with *N*=2 results in 19% error, whereas the *N*=4 error is less than 2%.

N	F_T	F_S	$err = \frac{F_T - F_T\big\rvert_{N=32}}{F_T\big\rvert_{N=32}}$
2	29.55387	50.23965	0.1899
4	25.28658	42.98554	0.0181
8	24.83962	42.22573	0.0001
16	24.83668	42.22074	$err < 10^{-5}$
32	24.83668	42.22074	NA

Table 1. Convergence of the Floquet based algorithm in a two-dimensional calculation for $(R_\rho, Pr, \tau) = (1.9, 7, 0.01)$. As the number of spectral harmonics (*N*) increases, the heat flux (F_T) rapidly approaches its limiting ($N \to \infty$) value.

B. THREE-DIMENSIONAL FORMULATION

Numerical simulations (e.g., Stern et al.,, 2001) reveal significant differences, in magnitude and dynamics, between two- and three-dimensional salt fingers. Three-dimensional fluxes are systematically higher, by a factor of 2-3, than their 2D counterparts. In this section, we attempt to extend the growth rate balance theory to three dimensions. In addition to the natural interest in three-dimensional dynamics—after all, we live in a three-dimensional world—we are also motivated by the expectation that the results will help to rationalize the difference in the intensity of salt fingers in 2D and 3D. Since the following theory is analogous to the two-dimensional case (Section A of Chapter III), it is presented in abbreviated form.

The essential difference between two- and three-dimensional dynamics stems from the more complicated structure of the salt finger elevator mode in 3D:

$$\begin{cases} \overline{T} = A_T \exp(\lambda_1 t)\phi(x,y) \\ \overline{S} = A_S \exp(\lambda_1 t)\phi(x,y) \\ \overline{w} = A_W \exp(\lambda_1 t)\phi(x,y), \end{cases} \tag{18}$$

where the horizontal planform function ϕ satisfies the Helmholtz equation $\nabla_H^2\phi + k^2\phi = 0$. In 3D, identical growth rates can be attained by various horizontal planforms. For instance, even if we limit our analysis to rectangular planforms $\phi = \cos(k_x x)\cos(k_y y)$, all possible configurations with

$$k_x^2 + k_y^2 = k_{\max}^2 \tag{19}$$

yield the maximum growth rates (λ_1) and therefore are a priori equivalent. The degeneracy of linear theory with respect to the planform selection is well known and can be resolved by invoking fundamentally nonlinear considerations. Proctor and Holyer (1986) and Radko and Stern (2000) examined the problem for a "bounded" configuration, in which finger layer was limited by rigid horizontal surfaces—the setup analogous to the classical Rayleigh convection problem. The former (latter) study suggested the tendency of the planform to evolve spontaneously to two-dimensional rolls (square cells). For the unbounded regime, some guidance regarding the planform selection was provided by diagnostics of numerical simulations in Radko and Stern (1999), which indicate the preferred planform is neither square nor a roll, but, rather, some combination thereof, perhaps best described by the planform function of the following type:

$$\phi = \cos(k_{\max} x) + \frac{1}{2}\cos(k_{\max} y), \tag{20}$$

which was used in all calculations described below. It should be mentioned, however, that for our purpose—determination of the equilibrium transport characteristics—the planform choice turns out not to be particularly significant, with the square cell model performing only slightly worse than Equation (20).[1]

---

[1] We also note in passing that sheared environments favor formation of salt sheets aligned in the direction of the background current (Linden, 1974; Kimura and Smyth, 2007), in which case salt finger dynamics become similar to the 2D case discussed in Sec. 3a. It is perhaps ironic that since large-scale shears are ubiquitous in the ocean, salt fingers may be better represented by two-dimensional than by three-dimensional simulations.

The calculation of secondary growth rates for the square salt fingers Equation (20) proceeds, as previously, by the method based on the Floquet theory. The governing equations, Equation (2), are linearized with respect to the basic state Equation (18); which is assumed to be maintained in a quasi-steady state, and the solution is sought in the following form:

$$\begin{pmatrix} T' \\ S' \\ u' \\ \mathrm{v}' \\ w' \\ p' \end{pmatrix} = \exp(if_x kx + if_y ky + imz + \lambda t) \sum_{n_x=-N}^{N} \sum_{n_y=-N}^{N} \begin{pmatrix} T_{n_x,n_y} \\ S_{n_x,n_y} \\ u_{n_x,n_y} \\ \mathrm{v}_{n_x,n_y} \\ w_{n_x,n_y} \\ p_{n_x,n_y} \end{pmatrix} \exp(in_x kx + in_y ky), \tag{21}$$

where (f_x,f_y) are the Floquet factors in *x* and *y*. Substituting Equation (21) in the linearized governing equations and collecting the individual Fourier components reduces the stability problem to matrix form Equation (13). Maximizing the growth rates with respect to (f_x,f_y,m), we predict the largest growth rates of secondary instabilities (λ_2) as a function of (R_ρ,Pr,τ,A_T). Finally, for any given *C*, we search for the amplitude $A_T = A_T^*$ that satisfies the growth rate balance Equation (1). The vertical fluxes are then reconstructed as follows:

$$\begin{cases} F_T = \overline{wT} = \dfrac{5}{8} A_T^2 \left(\lambda_1 + k_{\max}^2\right) \\ F_S = \overline{wS} = \dfrac{5}{8R_\rho} \dfrac{A_T^2 \left(\lambda_1 + k_{\max}^2\right)^2}{\left(\lambda_1 + \tau k_{\max}^2\right)} \end{cases} \tag{22}$$

and plotted in Figure 9 as a function of density ratio (R_ρ) for various values of *C*.

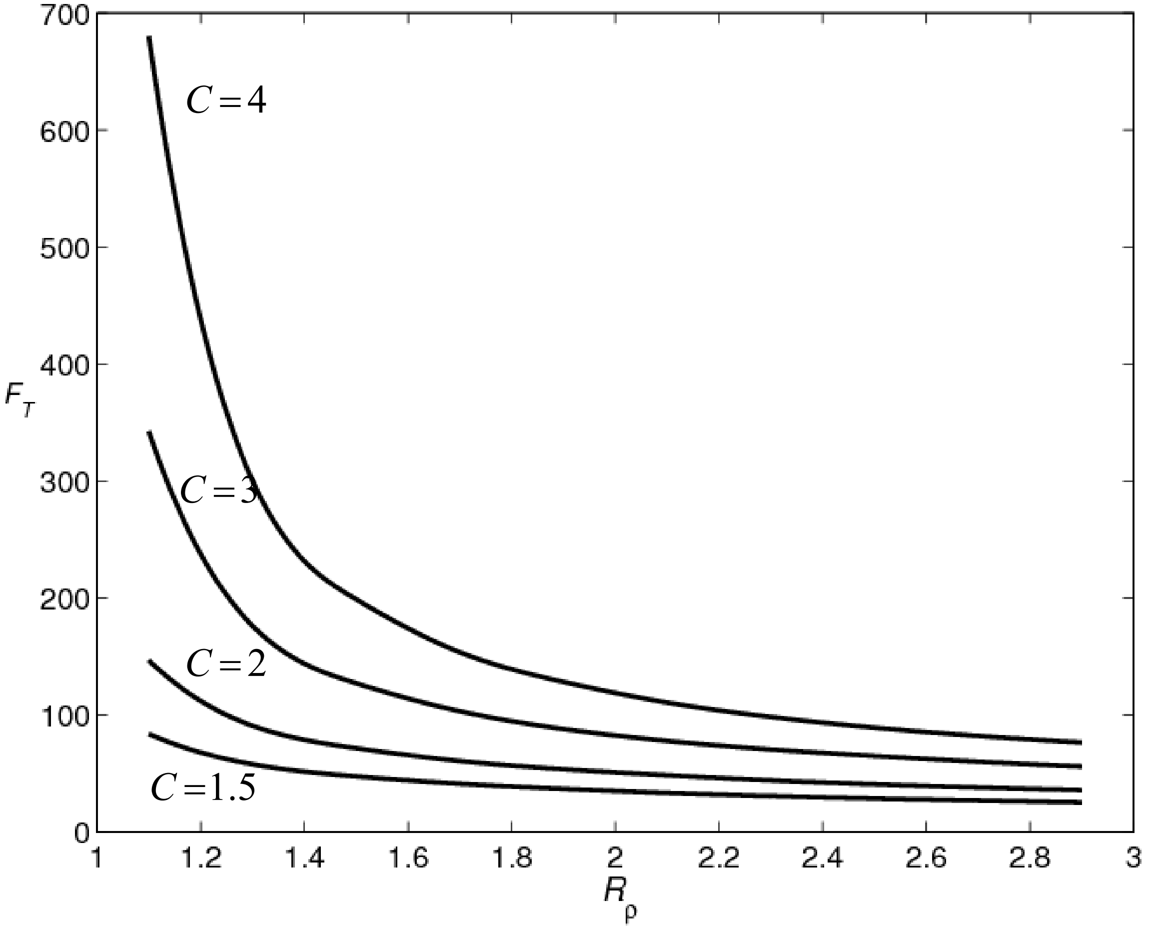

Figure 9. Heat flux in the theoretical three-dimensional model for various values of *C*.

While the patterns of 3D (Figure 9) and 2D (Figure 8) fluxes are qualitatively similar—in both cases fluxes rapidly reduce with R_ρ and increase with *C*—we note that the 3D fluxes are consistently higher. The reason is attributed to the fact that the 2D basic state Equation (9) is more unstable than its 3D counterparts Equation (18) and Equation (20). Thus, the amplitude of salt fingers has to be significantly higher in 3D to produce secondary instabilities of the same strength as in 2D, which rationalizes the behavior noticed in the numerical simulations of Stern et al., (2001).

IV. OCEANOGRAPHIC (HEAT-SALT) CASE: DNS ANALYSIS

In this chapter, we present numerical simulations of oceanographic double-diffusive convection, warm saltier water over colder fresher water, with density ratio (R_ρ) values 1.1, 1.3, …, 2.9 (Table 2). We have initiated these experiments by computer-generated small amplitude temperature and salinity distribution. Although double-diffusive interactions may lead to larger scale phenomena, such as thermohaline staircases, thermohaline intrusions, and internal waves (Traxler et al., 2011), this experiment only focuses on 10 individual fingers (5 warm/salty and 5 cool/fresh initially). The vertical salinity (F_S) and temperature (F_T) fluxes were recorded as a function of time and their statistical averages were analyzed as a function of density ratio. Simulations of this nature have only recently become possible, as computer technology has exceeded the petaflop barrier. This has allowed us to explore other parameter regimes besides just heat and salt interactions as discussed in Chapter V.

A. CALIBRATION OF THE THEORETICAL MODEL

A limitation of the theoretical model in Chapter III is related to its inability to determine the constant *C* internally. Our theory assumes that *C* is comparable to unity but does not provide an exact value. In order to calibrate *C*, we now turn to DNS. For the heat/salt case ($Pr=7,\tau=0.01$) discussed in this section, the analysis is based on 10 two-dimensional and 10 three-dimensional simulations conducted for $R_\rho = 1.1,1.3,\ldots,2.9$.

Figure 10 presents fluxes from a series of two-dimensional calculations, plotted along with the theoretical prediction from the foregoing growth rate balance theory (Chapter II) with C=4.3. In all simulations we used $(N_x,N_z)=(256,512)$ grid points and the size of the computational domain $(L_x,L_z)=(38.2,76.3)$ equivalent to 5 x 10 linearly fastest growing finger wavelengths (*d*). The variation of heat (Figure 10a) and salt (Figure 10b) fluxes with density ratio follows the theoretical pattern very closely. The ability of our model, containing only one adjustable parameter, to capture the details of the numerical simulations to such an extent lends credence to the proposed condition Equation (1) as the most relevant physical factor constraining growth of salt fingers.

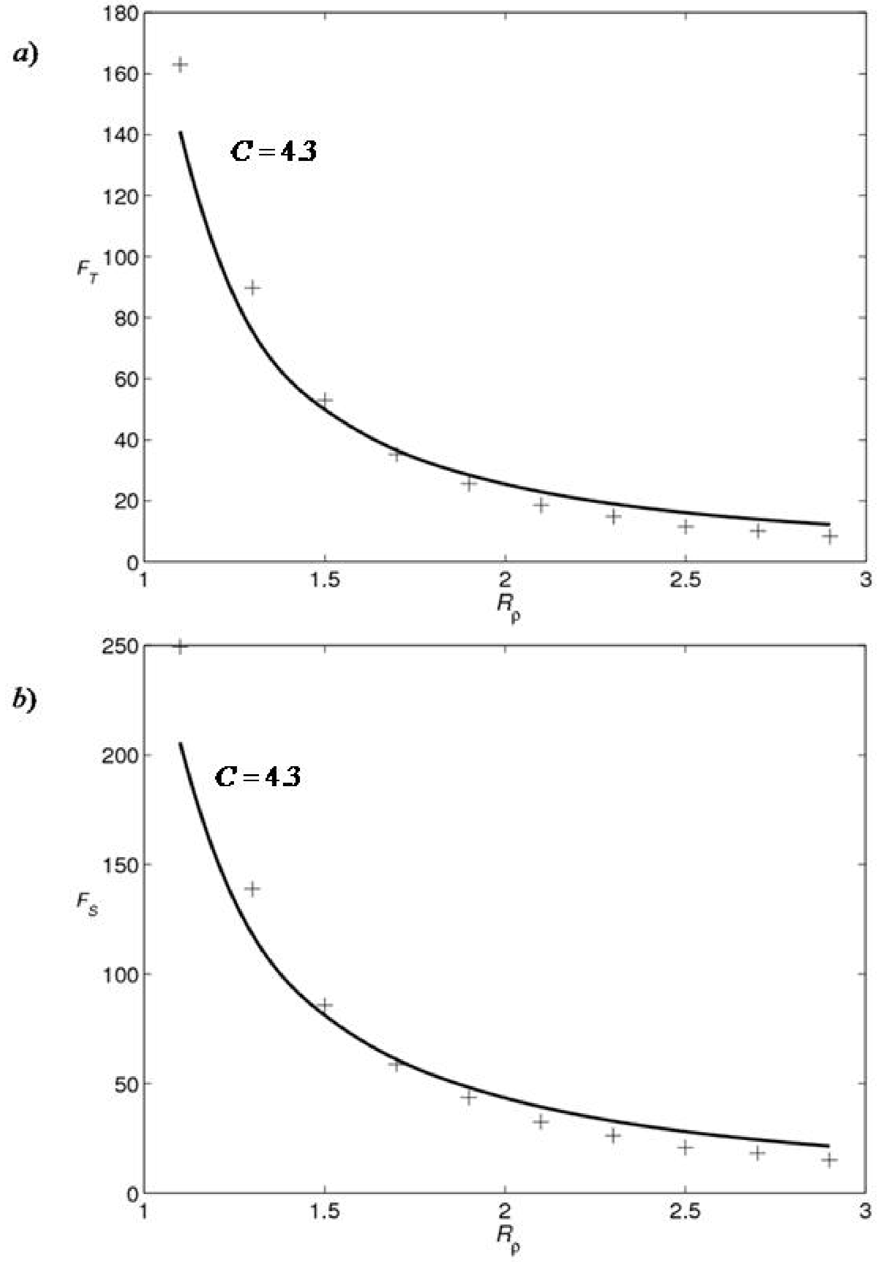

Figure 10. Comparison of the theoretical two-dimensional model for *C*=4.3 (solid curve) with DNS (plus signs). Heat and salt fluxes are shown in *a*) and *b*) respectively.

Figure 11 presents the corresponding three-dimensional calculations. The resolution of three-dimensional DNS matched the two-dimensional runs: (N_x,N_y,N_z)=(256,256,512) mesh was used to resolve 5x5x10 fastest growing finger wavelengths. The theoretical calculation for *C*=2.7 is superimposed on the numerical data, revealing their mutual consistency—our theory predicts the right order of magnitude and the pattern of fluxes as a function of R_ρ. The relevant value of the adjustable coefficient C=2.7 in 3D is comparable to—but differs from—the 2D value of C=4.3. The (limited) variation in C can be readily attributed to distinct equilibrium dynamics of three-dimensional and two-dimensional salt fingers in the unbounded model (Radko and Stern 1999).

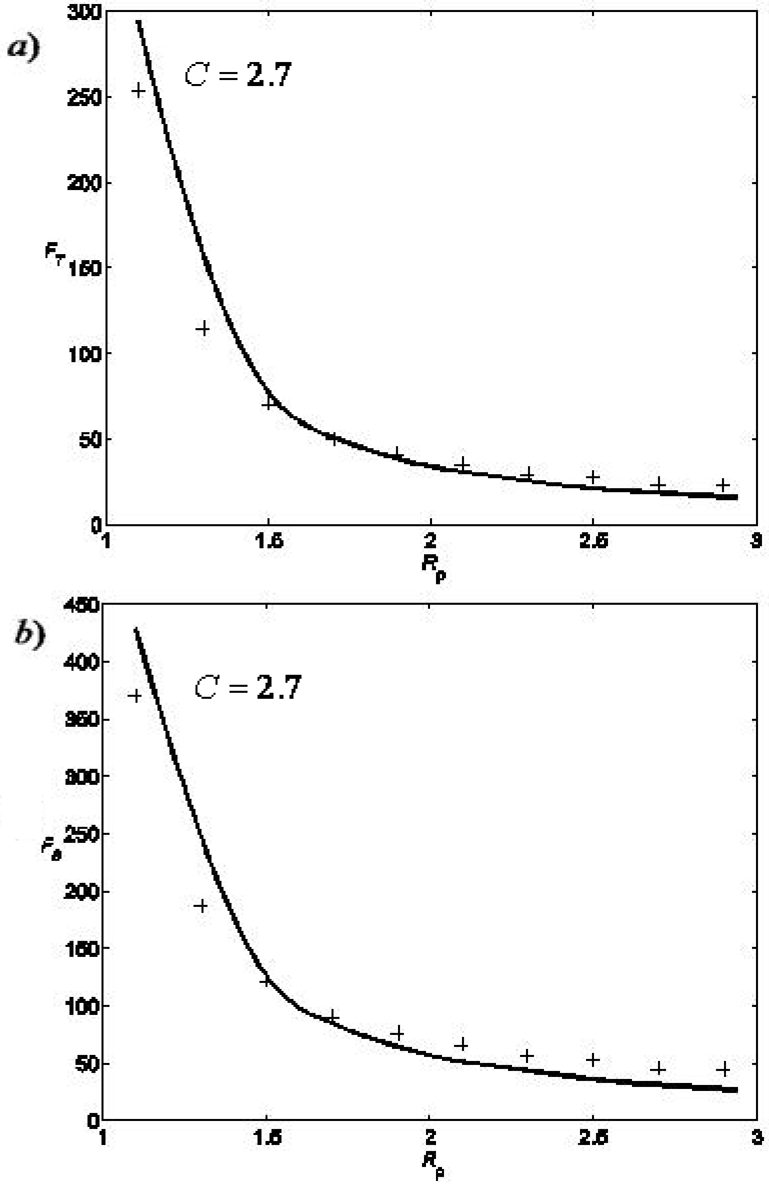

Figure 11. The same as in Figure 10 but for the three-dimensional model with C=2.7.

B. OBSERVED PATTERNS

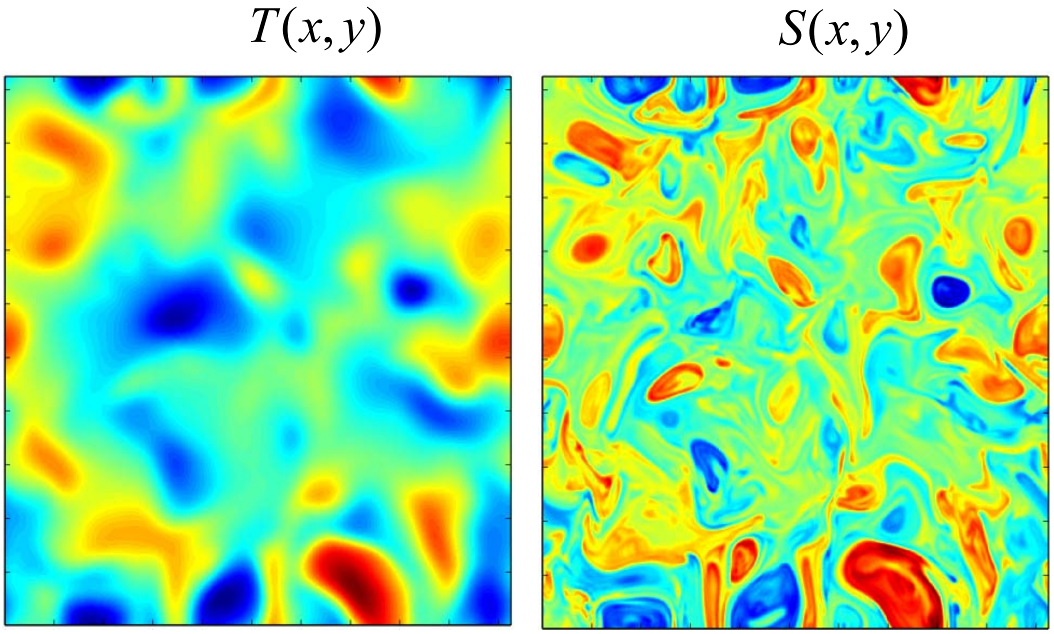

$T(x,y)$ $S(x,y)$

Figure 12. Horizontal distribution of temperature and salinity for fully equilibrated state. Oceanographic values of Pr = 7, $\tau = 0.01$, $R_\rho = 1.9$.

The horizontal and vertical structure of individual fingers can be clearly seen from Figures 12 and 13, respectfully. It is interesting to note that the temperature field is characterized by much larger scales than that of salinity. It is also evident that while both the temperature and salinity distributions are spatially correlated there is more variability within the salinity field. This latter feature is due to the fact that salinity diffuses on much smaller scales (100 times slower) than temperature.

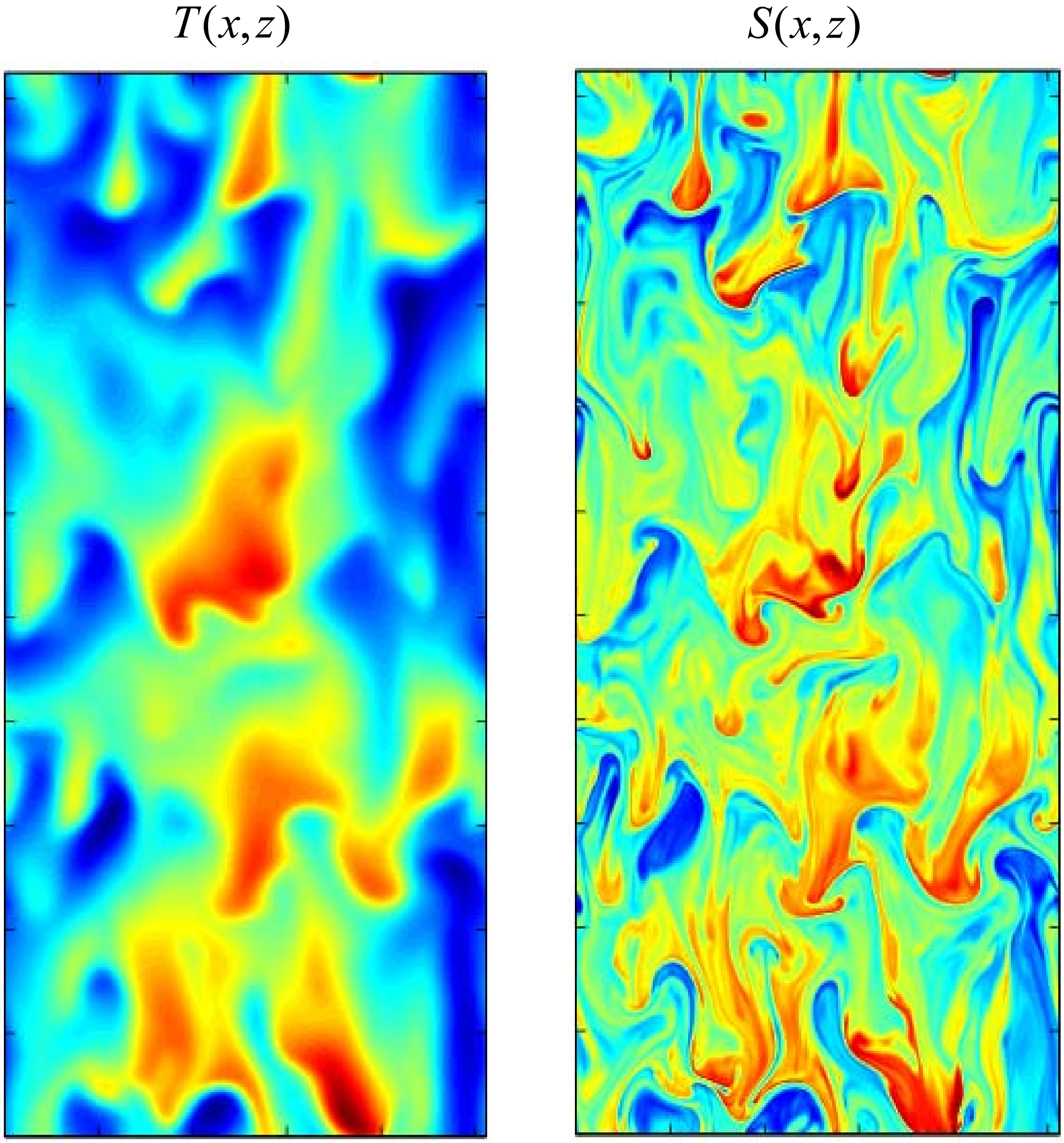

$T(x,z)$ $S(x,z)$

Figure 13. Vertical distribution of temperature and salinity for the fully equilibrated state. Oceanographic values of Pr = 7, $\tau = 0.01$, $R_\rho = 1.9$.

C. MIXING CHARACTERISTICS

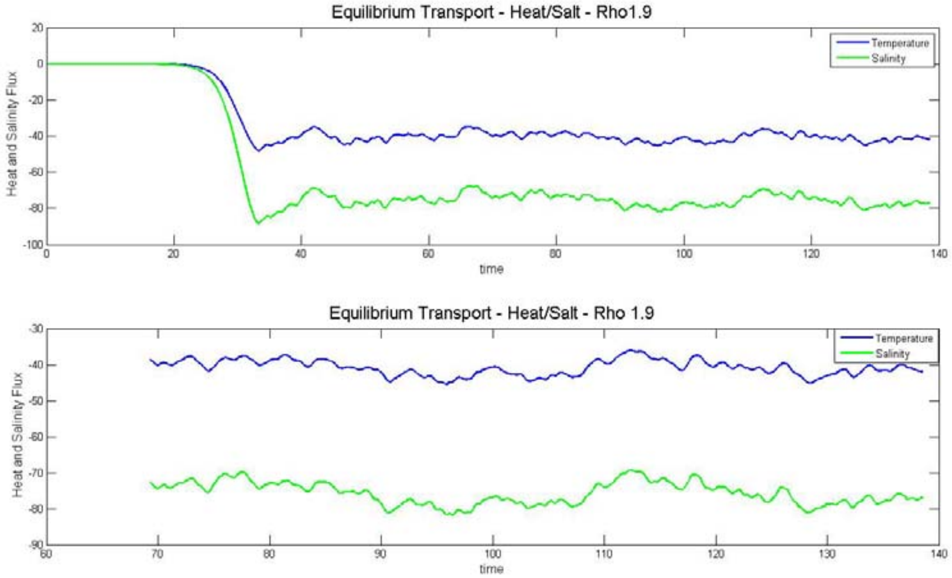

Figure 14. Temperature and salinity fluxes as a function of time for the heat-salt case. F_T and F_S values are calculated after equilibrium is reached.

Temperature and salinity fluxes for a typical North Atlantic oceanographic case ($Pr = 7$, $\tau = 0.01$, $R_\rho = 1.9$) are plotted in Figure 14. Note that fluxes in Figure 14 are given in dimensional units and the sign convention reflects downward transport of heat and salt (unlike Figure 5). Our model starts using random noise until equilibrium is reached and the data for oceanographic applications are taken from the fully equilibrated stage (lower panel of Figure 14).

Using data similar to that in Figure 14 for a range of R_ρ, we can calculate a mean of our fluxes after equilibrium is reached. This corresponds to typical conditions in the Atlantic thermocline for a range of density ratio values (R_ρ). These values are included in Table 2, along with the dimensional temperature and salinity diffusivities (K_{Tdim} and K_{Sdim}) which are of the same order of magnitude expected in the ocean. Also included in Table 2 are Buoyancy Flux ($F_S - F_T$) and Flux Ratio ($\gamma = \frac{F_T}{F_S}$) values for the heat salt case.

Heat/Salt 256x256x512						
R_ρ	**F_T**	**F_S**	**K_{Tdim}(m^2/s)**	**K_{Sdim}(m^2/s)**	**Buoyancy Flux**	**Ratio**
1.1	-253.3917	-369.8733	-3.471E-05	-5.574E-05	116.4816	0.685077025
1.3	-114.1179	-186.4594	-1.563E-05	-3.321E-05	72.3415	0.61202546
1.5	-70.2319	-121.8825	-9.622E-06	-2.505E-05	51.6506	0.576226284
1.7	-49.5589	-90.2265	-6.790E-06	-2.101E-05	40.6676	0.54927211
1.9	-40.8760	-75.8794	-5.600E-06	-1.975E-05	35.0034	0.538696932
2.1	-35.0073	-65.8659	-4.796E-06	-1.895E-05	30.8586	0.531493535
2.3	-28.9132	-56.0535	-3.961E-06	-1.766E-05	27.1403	0.515814356
2.5	-27.3972	-52.2506	-3.753E-06	-1.790E-05	24.8534	0.524342304
2.7	-23.0670	-45.2340	-3.160E-06	-1.673E-05	22.1670	0.509948269
2.9	-22.7098	-44.1900	-3.111E-06	-1.756E-05	21.4802	0.51391265

Table 2. Heat - Salt temperatures (F_T) and salinity (F_S) fluxes for a range of density ratios, Rρ. Also shown are the dimensionalized temperature and salinity diffusivities (K_{Tdim}, K_{Sdim}), Buoyancy Flux (F_S-F_T), and Flux Ratio (F_T/F_S).

While development of explicit parameterizations of double diffusion for large-scale ocean modeling is outside of our immediate goal, it could prove beneficial for more applied studies to note that the numerical data in Figure 11 can be accurately approximated by the following algebraic expressions:

$$\begin{cases} F_S = \dfrac{a_S}{\sqrt{R_\rho - 1}} + b_S, & (a_S, b_S) = (135.7, -62.75) \\ \gamma = a_\gamma \exp(-b_\gamma R_\rho) + c_\gamma, & (a_\gamma, b_\gamma, c_\gamma) = (2.709, 2.513, 0.5128) \\ F_T = \gamma F_S, & \end{cases} \tag{23}$$

which are indicated in Figure 15 by the red curve. The structure of the expression for $F_S(R_\rho)$ is suggested by theoretical arguments in Radko (2008), whereas the expression for the flux ratio $\gamma(R_\rho)$ represents a purely empirical exponential fit to the numerical data.

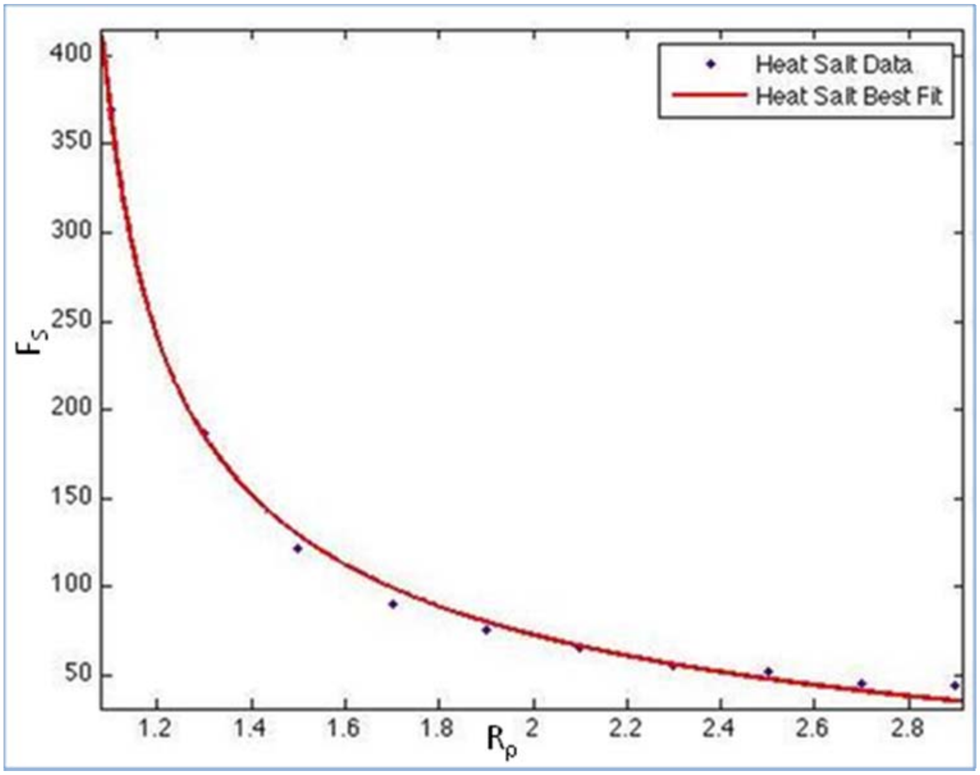

Figure 15. The best fit for Heat Salt (Pr=7; τ=0.01) utilizing cftool in MATLAB to solve Equation (23).

V. GENERALIZATIONS

In this section, we go beyond the oceanographically motivated heat-salt $(Pr,\tau)=(7,0.01)$ case and test the generality of our conclusions by exploring a broader parameter range. The discussion in this section is based on the comparison of four representative series of three-dimensional numerical experiments with corresponding theoretical results:

- Case 1: Low Prandtl number $(Pr,\tau)=(0.1,0.01)$;
- Case 2: High Prandtl number $(Pr,\tau)=(100,0.01)$;
- Case 3: High diffusivity ratio $(Pr,\tau)=(7,0.1)$;
- Case 4: High Prandtl number and High diffusivity ratio$(Pr,\tau)=(1000,1/3)$;

Unfortunately, DNS for more extreme parameter values ($Pr\rightarrow\infty$, $Pr\rightarrow 0$, $\tau\rightarrow 0$) become computationally prohibitive in 3D. However, our selection represents a substantial fraction of the numerically accessible range. In all cases, we performed a series of calculations with R_ρ = 1.1,1.3,…,2.9 in computational domains corresponding to 5 x 5 x 10 fastest growing finger wavelengths, recording the average equilibrium fluxes.

Comparing Case 1 with our baseline heat-salt configuration allows us to examine specifics of the low Prandtl number regime, which is relevant for astrophysical applications. Likewise, differences between Case 2 and heat-salt provide some glimpse into the large Prandtl number regime, exemplified by double-diffusion in magma chambers. Case 3 differs from the heat-salt calculation by diffusivity ratio, which also varies dramatically between various applications—from τ = 0.8 for heat/humidity in the atmosphere to $\tau\sim 10^{-6}$ in stellar interiors. Finally, Case 4 (Sugar Salt parameters) is a combination of an increase in Prandtl number and diffusivity ratio and behaves differently than the majority of runs throughout our experiments, but is referenced to show how these differences in parameters affect results.

Density Ratio ***R_ρ = 1.9***	Pr	τ	F_T	F_S
Heat-Salt	7	0.01	-40.8760	-75.8794
Case 1	0.1	0.01	-1.9140	-4.6501
Case 2	100	0.01	-220.1848	-364.8436
Case 3	7	0.1	-39.3424	-60.2595
Case 4	1000	1/3	-769.4803	-885.3976

Table 3. Dependence of the equilibrium *T*-*S* fluxes on the molecular characteristics (Pr,τ) in three-dimensional simulations with R_ρ=1.9.

A. OBSERVED PATTERNS

We can gain a qualitative understanding of the effects of parameter changes by reviewing Figures 16 to 19. We note that for each of these figures, the equilibrium point has already been reached.

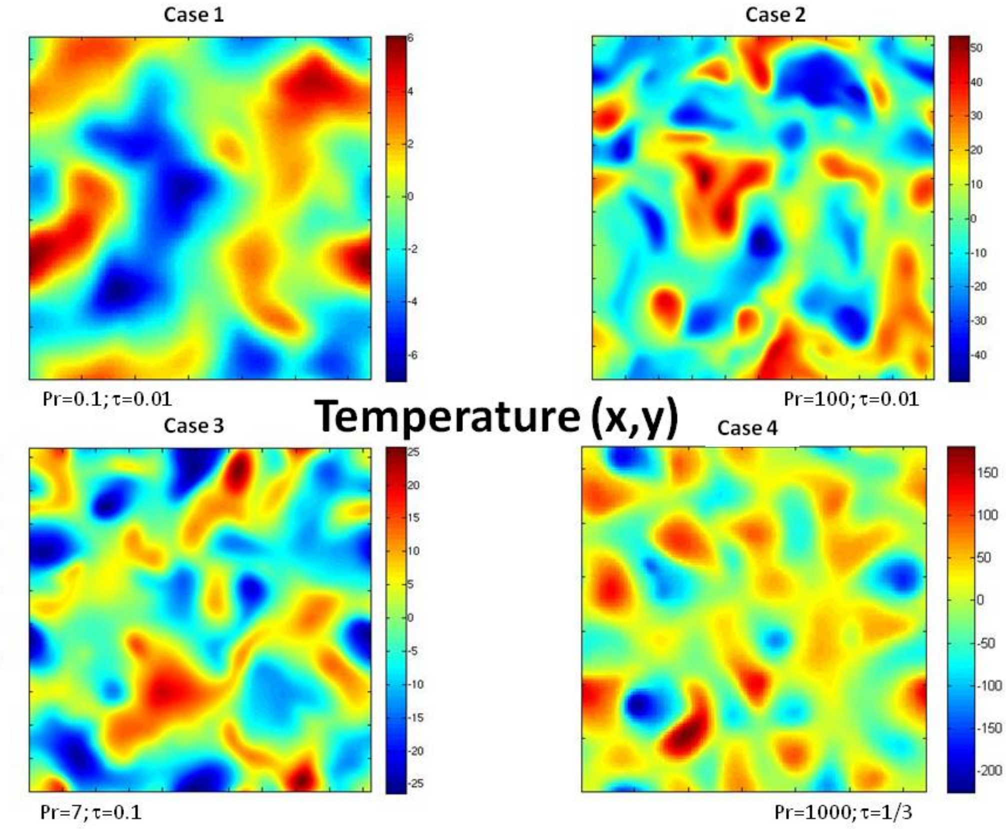

Figure 16. DNS model of horizontal temperature (highest rate of diffusion) in (x, y) coordinates for Cases 1 through 4.

Taking a horizontal slice of the temperature field (Figure 16) allows us to further explore the similarities and changes in fingers caused by differences in background parameters. It can be seen that there exists decreasing dependence between Prandtl number and horizontal finger scales.

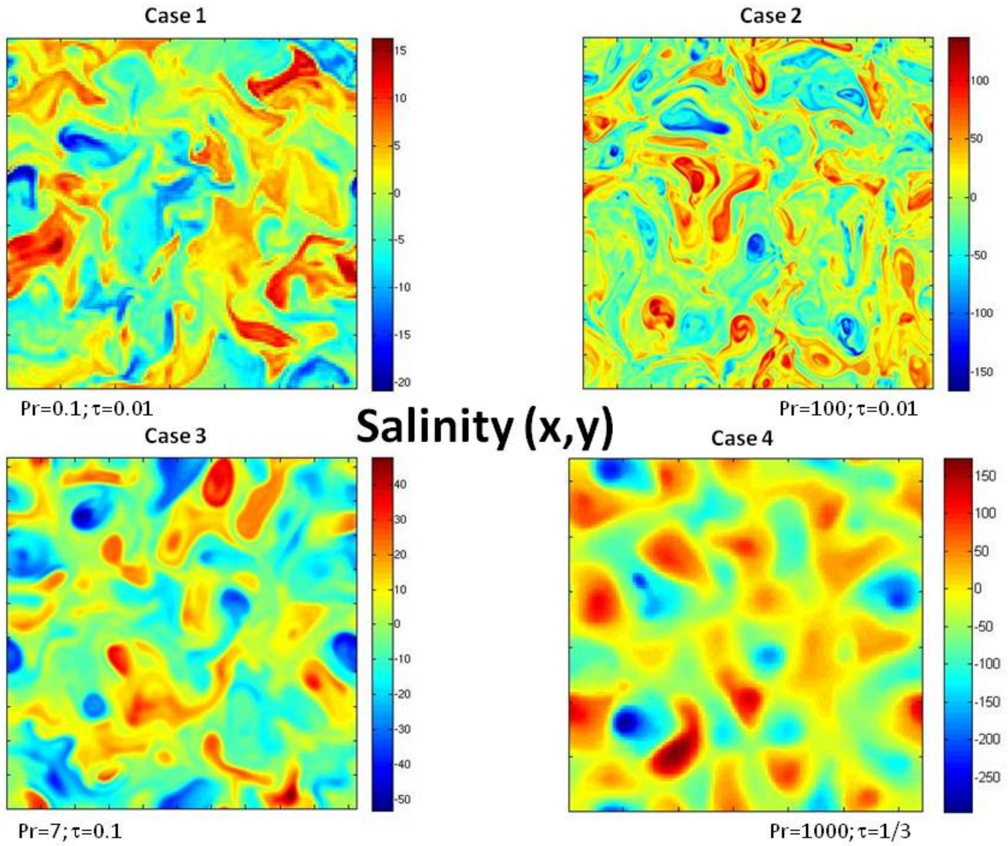

Figure 17. DNS model of horizontal salinity (least rate of diffusion) in (x,y) coordinates for Cases 1 through 4.

At first glance, a review of the horizontal sections of salinity fields (Figure 17) does not show as clear cut of a correlation as that of temperature fields. By breaking the analysis down into groups, where we hold some parameters constant, we begin to see a pattern emerge. For example, from comparison of heat-salt (Figure 12) with cases 1 and 2, where $\tau = 0.01$ and the Prandtl number changes from 7, 0.1, to 100, it can be seen that indeed diameter size increases with a decrease in Prandtl number. We can also examine cases where the Prandtl number remains constant and the diffusivity ratio varies, by comparing heat-salt and Case 3 (where τ increases from 0.01 to 0.1). It is readily observed that increased τ results in increased finger scales.

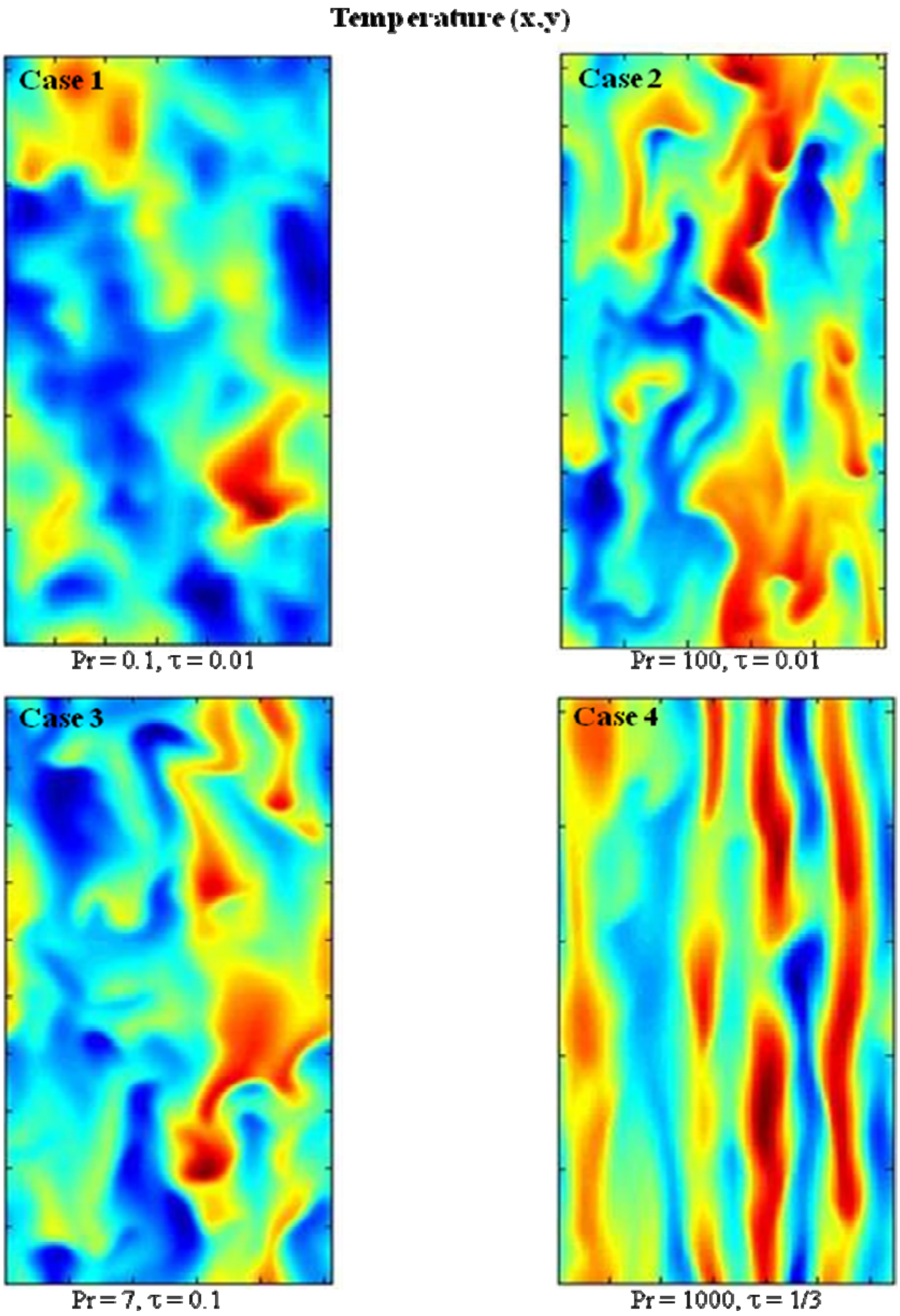

Figure 18. DNS model of vertical temperature (fastest rate of diffusion) in (x, z) coordinates.

In addition to what has been observed in the temperature field (horizontal) section example (Figure 16), we can now examine finger length scales and their dependencies from the vertical sections of the temperature fields (Figure 18). It is clear that thinner, longer fingers occur for higher Prandtl numbers. This graphic shows that a decrease in Prandtl number and an increase in the diffusivity ratio both cause a less defined finger formation.

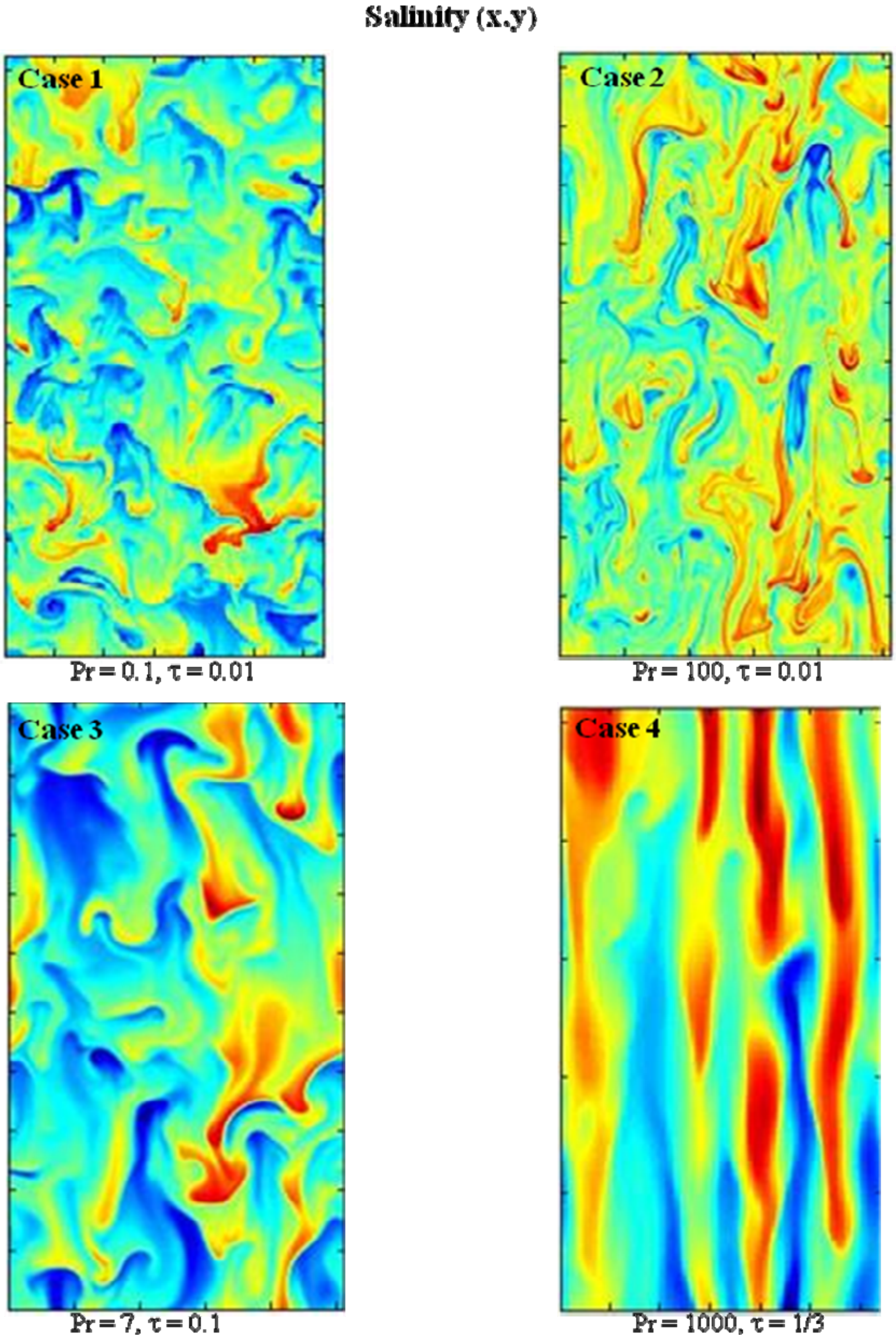

Pr = 0.1, τ = 0.01

Pr = 100, τ = 0.01

Pr = 7, τ = 0.1

Pr = 1000, τ = 1/3

Figure 19. DNS model of vertical salinity (slowest rate of diffusion) in (x, z) coordinates.

Visual inspection of the vertical salinity sections in Figure 19 supports the foregoing inferences. Comparing heat-salt with Cases 2 and 4 implies that an increase in Prandtl number results in thinner, longer individual fingers. Magma chamber fingers (with large Prandtl values) have been observed in laboratory experiments as being slim or slender (Tait 1989) and is verified by these results. A more objective measure of the previously observed patterns of salt fingers is given by the aspect ratio:

$$A_R = \frac{<T_X^2 + T_Y^2 + T_Z^2>}{3<T_Z^2>} \tag{24}$$

This quantity reduces to one in the limit of isotropic fingers and increases as fingers become more elongated. Comparison of heat salt and Case 3 (one order of magnitude increase in diffusivity ratio) shows only a slight increase in the aspect ratio (A_R). A summary of the dependencies of A_R is shown in Figure 20 and in Table 4.

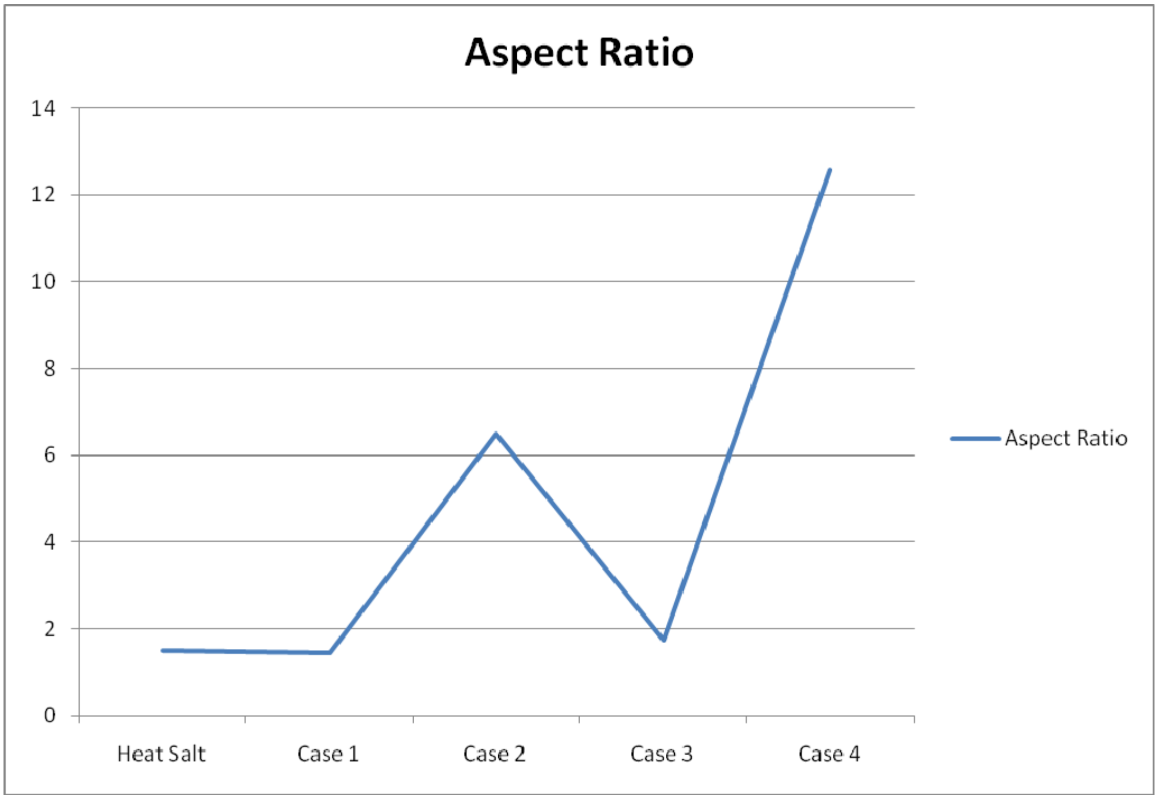

Figure 20. Aspect Ratio, Equation (24), for $R_\rho = 1.9$ for Heat Salt and Cases 1 to 4.

Aspect Ratio at Rρ=1.9				
Heat Salt	Case 1	Case 2	Case 3	Case 4
1.4928	1.4349	6.5011	1.7506	12.5670

Table 4. Aspect Ratio of Heat - Salt and Cases 1 through 4.

For the same density ratio, R_ρ = 1.9, (Figure 20 and Table 4) the aspect ratio increases with an increase in Prandtl number. As τ increases, the aspect ratio increases slightly as reflected by the differences between the heat salt case and Case 3.

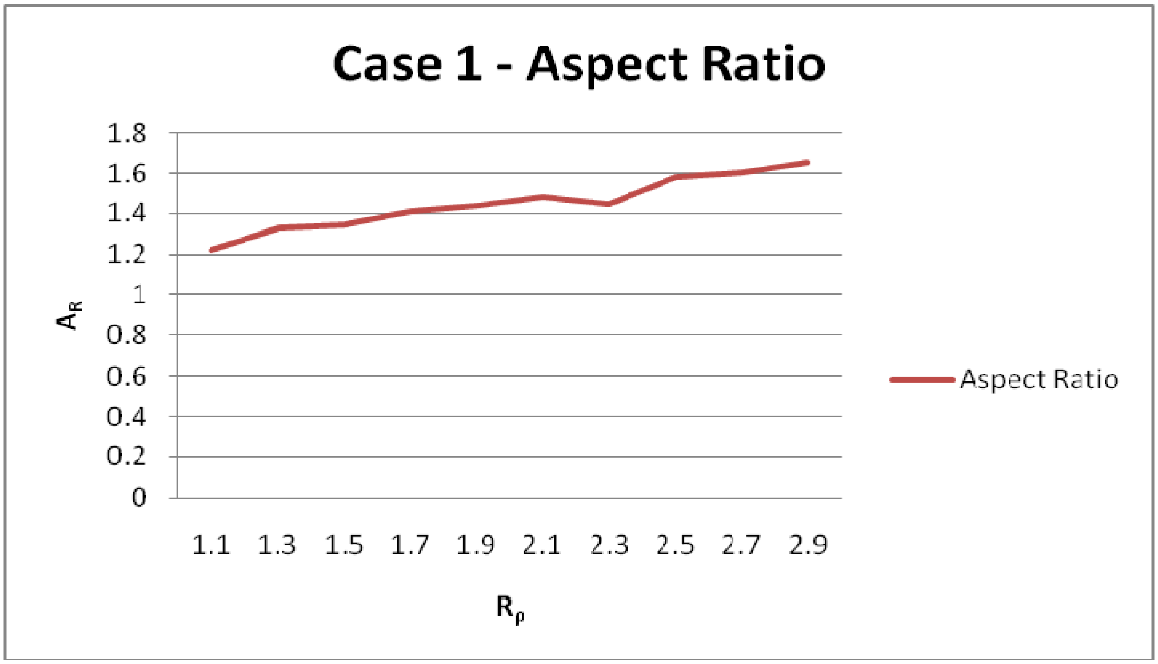

Figure 21. Case 1 Aspect Ratio as a function of Density Ratio.

Examination of Case 1(Figure 21 and Table 5), in which Pr and τ are held constant throughout a wide range of $R_{\rho,}$ reveals that an increase in density ratio is accompanied by a monotonic increase in aspect ratio.

Case 1	
R_ρ	A_R
1.1	1.2261
1.3	1.3271
1.5	1.3453
1.7	1.4101
1.9	1.4349
2.1	1.4796
2.3	1.4489
2.5	1.5791
2.7	1.6038
2.9	1.6564

Table 5. Aspect Ratio as a function of density ratio values in Case 1.

B. TRANSPORT CHARACTERISTICS

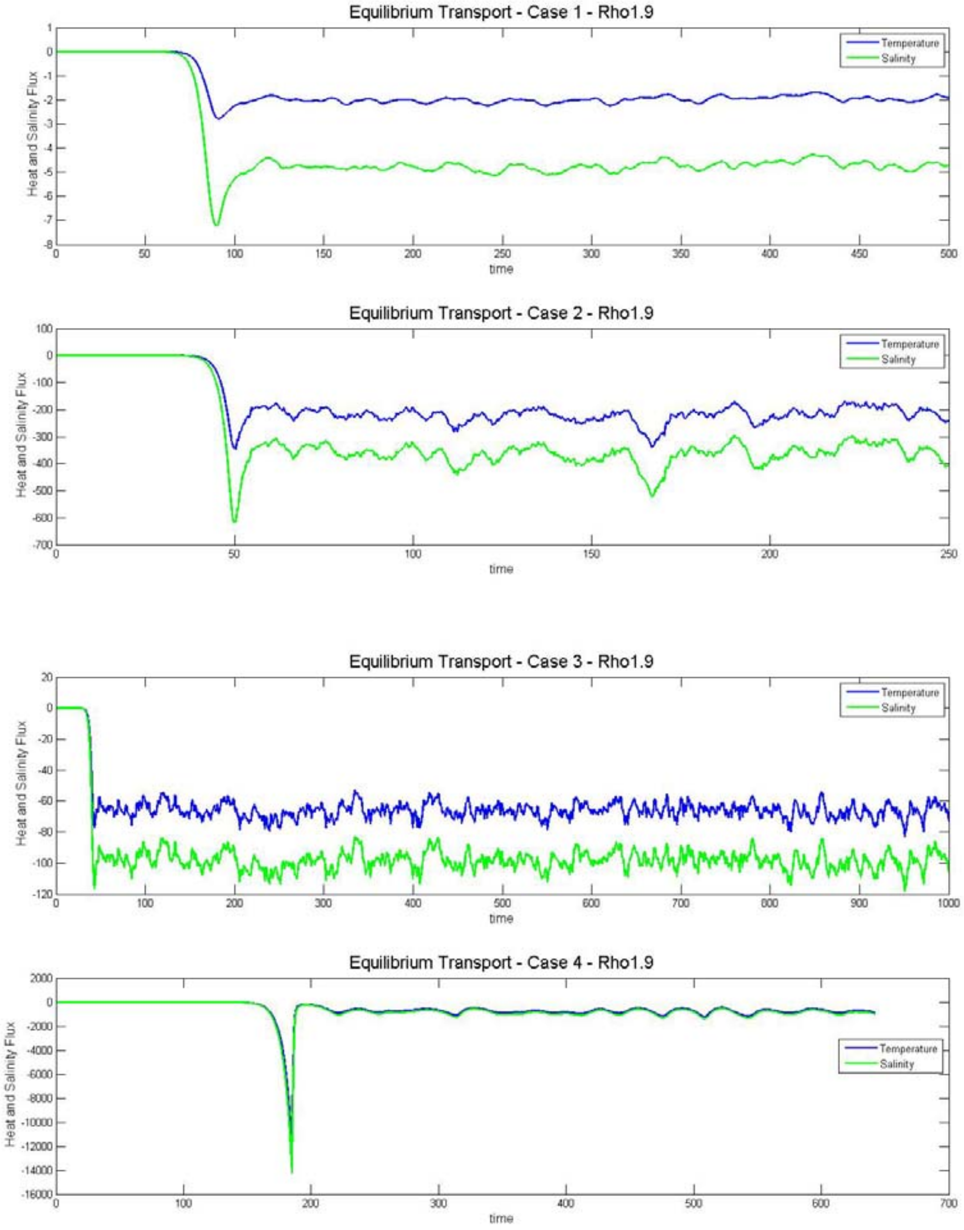

Figure 22. Temperature and salinity fluxes as a function of time for cases 1 through 4.

Case #1				
Rρ	**F_T**	**F_S**	**Buoyancy**	**Ratio**
1.1	-6.4812	-14.4047	7.9235	0.449936
1.3	-4.1979	-9.8905	5.6926	0.424438
1.5	-3.1962	-7.4937	4.2975	0.426518
1.7	-2.581	-6.0696	3.4886	0.425234
1.9	-1.914	-4.6501	2.7361	0.411604
2.1	-1.6215	-3.8882	2.2667	0.417031
2.3	-1.4437	-3.4342	1.9905	0.420389
2.5	-1.2994	-3.0476	1.7482	0.426368
2.7	-1.0685	-2.5368	1.4683	0.4212
2.9	-0.9298	-2.1956	1.2658	0.423483

Case #2				
Rρ	**F_T**	**F_S**	**Buoyancy**	**Ratio**
1.1	-1105.08	-1478.96	373.8807	0.7472
1.3	-468.524	-705.2	236.6764	0.664384
1.5	-315.245	-499.912	184.6674	0.6306
1.7	-242.235	-398.488	156.2523	0.607887
1.9	-220.185	-364.844	144.6589	0.603505
2.1	-196.214	-328.582	132.3677	0.597154
2.3	-169.363	-282.033	112.6701	0.600507
2.5	-168.507	-286.134	117.6272	0.588908
2.7	-144.364	-245.818	101.4536	0.587281
2.9	-149.324	-250.356	101.0315	0.596448

Case #3				
Rρ	**F_T**	**F_S**	**Buoyancy**	**Ratio**
1.1	-234.914	-324.005	89.0909	0.725032
1.3	-104.725	-150.178	45.453	0.697339
1.5	-66.5649	-98.8597	32.2948	0.673327
1.7	-49.8729	-75.2535	25.3806	0.662732
1.9	-39.3424	-60.2595	20.9171	0.652883
2.1	-33.3554	-51.4704	18.115	0.64805
2.3	-26.356	-41.2481	14.8921	0.638963
2.5	-12.2223	-20.0053	7.783	0.610953
2.7	-15.3988	-25.0506	9.6518	0.614708
2.9	-12.0376	-19.733	7.6954	0.610024

Case #4				
Rρ	**F_T**	**F_S**	**Buoyancy**	**Ratio**
1.1	-3009.76	-3407.43	397.6623	0.883295
1.3	-1112.64	-1321.63	208.9909	0.841869
1.5	-873.25	-1047.29	174.0426	0.833817
1.7	-870.275	-1032.55	162.271	0.842844
1.9	-769.48	-885.398	115.9173	0.869079
2.1	-868.552	-983.512	114.9605	0.883112
2.3	-650.989	-720.552	69.5631	0.903459
2.5	-578.38	-626.742	48.3624	0.922835
2.7	-328.609	-344.985	16.3752	0.952534
2.9	-14.0786	-14.4201	0.3415	0.976318

Table 6. Tables of DNS results for all cases including average temperatures (F_T) and salinity (F_S) fluxes, buoyancy ($F_S – F_T$) and flux ratio (F_T/F_S).

Typical evolutionary patterns of temperature and salinity fluxes (not necessarily representing temperature and salinity) are presented in Figure 22, for $R_\rho = 1.9$. The summary of all calculations in Table 6 indicate that fluxes are most strongly affected by variation in the density ratio (R_ρ). Our limited numerical exploration of the effects of the molecular parameters suggests that, for any given R_ρ, fluxes increase with the Prandtl number (Pr) and very mildly decrease with the diffusivity ratio (τ)—see Tables 3 and 6. These dependencies are consistent with the prediction based on the growth rate balance model.

The purpose of the following calculation is to determine whether the empirical parameterization (Equation (23)) developed for the oceanographic heat salt case applies equally well to other configurations. This parameterization was applied to each case, using the cftool in MATLAB. Results are summarized in Table 7 (with quality of the fit indicated in the last column) and Figure 23.

Empirical Parameterization						
	a_s	b_s	a_γ	b_γ	c_γ	Goodness Of Fit
Heat Salt	135.7	-62.75	2.708	2.513	0.5128	99.7%
Case 1	5.113	-0.7788	427.7	8.738	0.4212	95.9%
Case 2	503.9	-160.6	8.649	3.663	0.5928	99.0%
Case 3	124.6	-72.75	0.359	0.8303	0.5772	99.8%
Case 4	1189	-482.2	N/A	N/A	N/A	93.5%

Table 7. Empirical parameterization of the temperature and salinity fluxes. Parameterization of the flux ratio for Case 4 has not been attempted due to the nonmonotonic pattern of $\gamma(R_\rho)$, which is inconsistent with the assumed expression, Equation (23).

Results in all cases are encouraging, suggesting the universal character of the assumed parameterization similar to Equation (23), as quantified by the goodness of fit for all simulations. Examining Table 7 shows the Prandtl number value has a significant effect on the magnitude of the a_s and b_s coefficients: as Prandtl number increases so do the magnitude of these values.

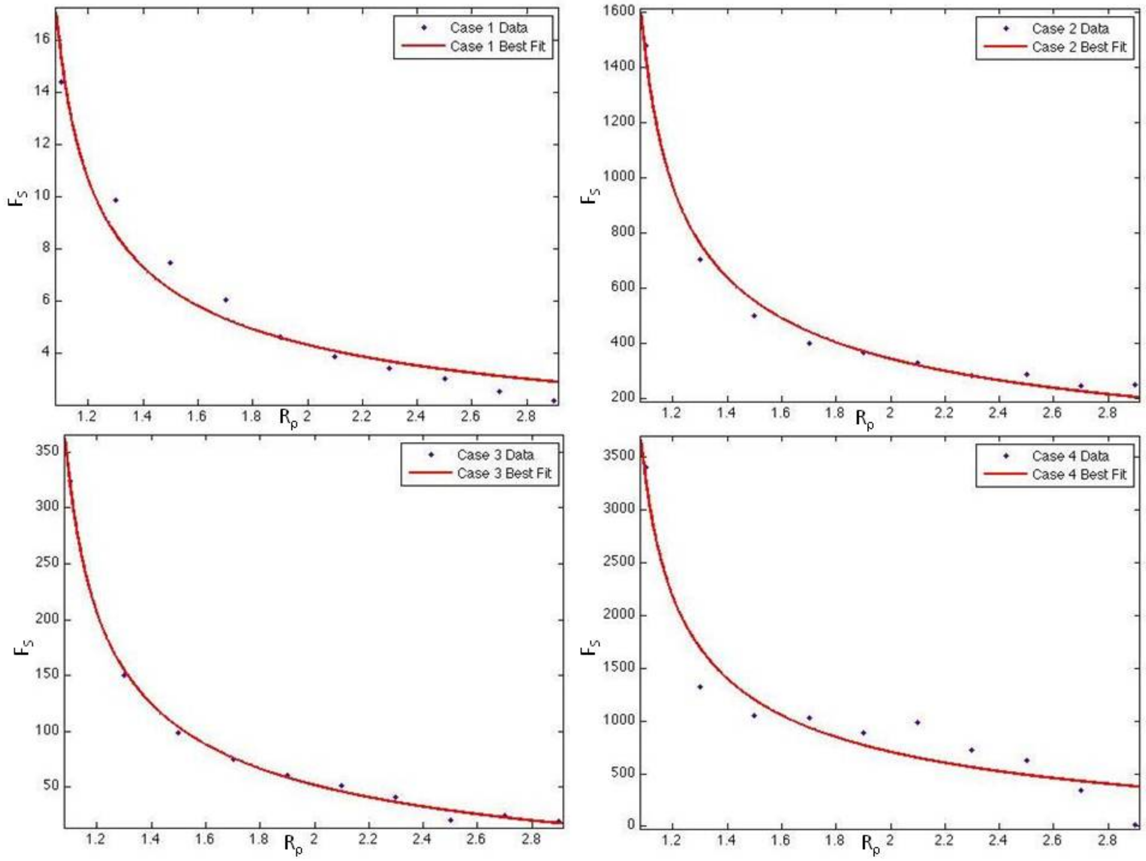

Figure 23. Best fit plots for Table 7, Cases 1 through 4, respectively. Compare to Heat Salt Best Fit (Figure 15).

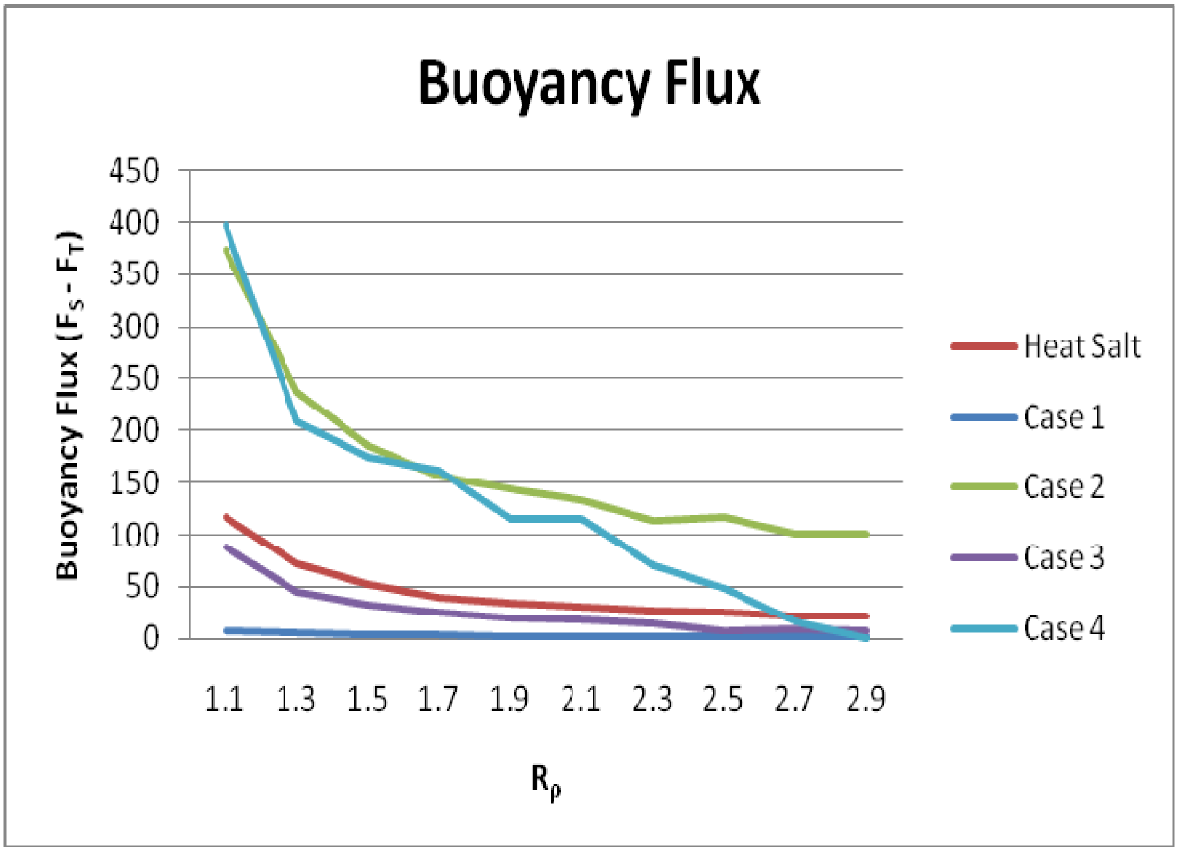

Figure 24. Buoyancy flux (F_S - F_T) is plotted showing that as R_ρ increases buoyancy decreases. This is an indirectly proportional relationship.

One of the key characteristics of fully developed salt fingering is related to its ability to transport buoyancy in the vertical direction. This characteristic is thought to be involved in the generation and maintenance of thermohaline staircases (Merryfield, 2000). The buoyancy flux values of the cases presented in this study (F_S - F_T) are examined in Figure 24, which reveals that an increase in R_ρ results in a decrease in the buoyancy.

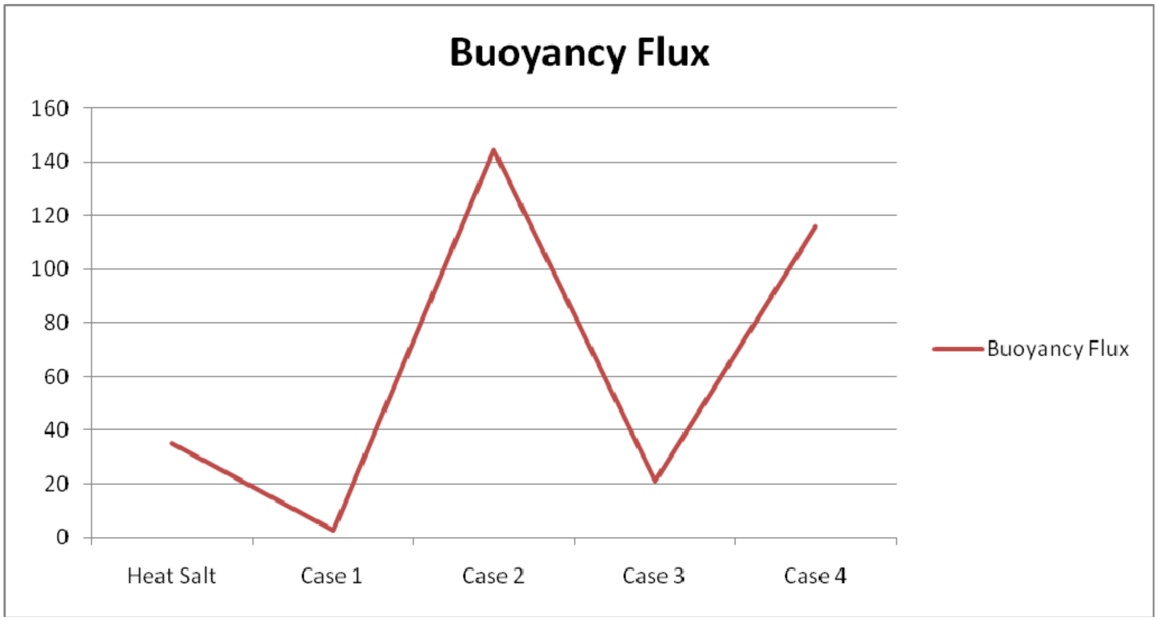

Figure 25. Buoyancy flux for each case at $R_\rho = 1.9$.

By taking a closer look at all cases at a fixed density ratio, $R_\rho = 1.9$, (Figure 25 and Table 8) we can see the two largest Prandtl number values in cases 2 and 4 (Pr = 100 and Pr = 1000 respectively) have the largest buoyancy values. In comparing the heat salt and Case 3 in which only the diffusivity ratio changes ($\tau = 0.01$ and $\tau = 0.1$, respectively) there is a slightly smaller buoyancy value for Case 3. Finally, in comparison of heat salt and Case 1, with a decrease in Prandtl number, the buoyancy decreases.

Buoyancy flux at R_ρ=1.9				
Heat Salt	Case 1	Case 2	Case 3	Case 4
35.0034	2.7361	144.6589	20.9171	115.9173

Table 8. Buoyancy flux at $R_\rho = 1.9$ of all cases.

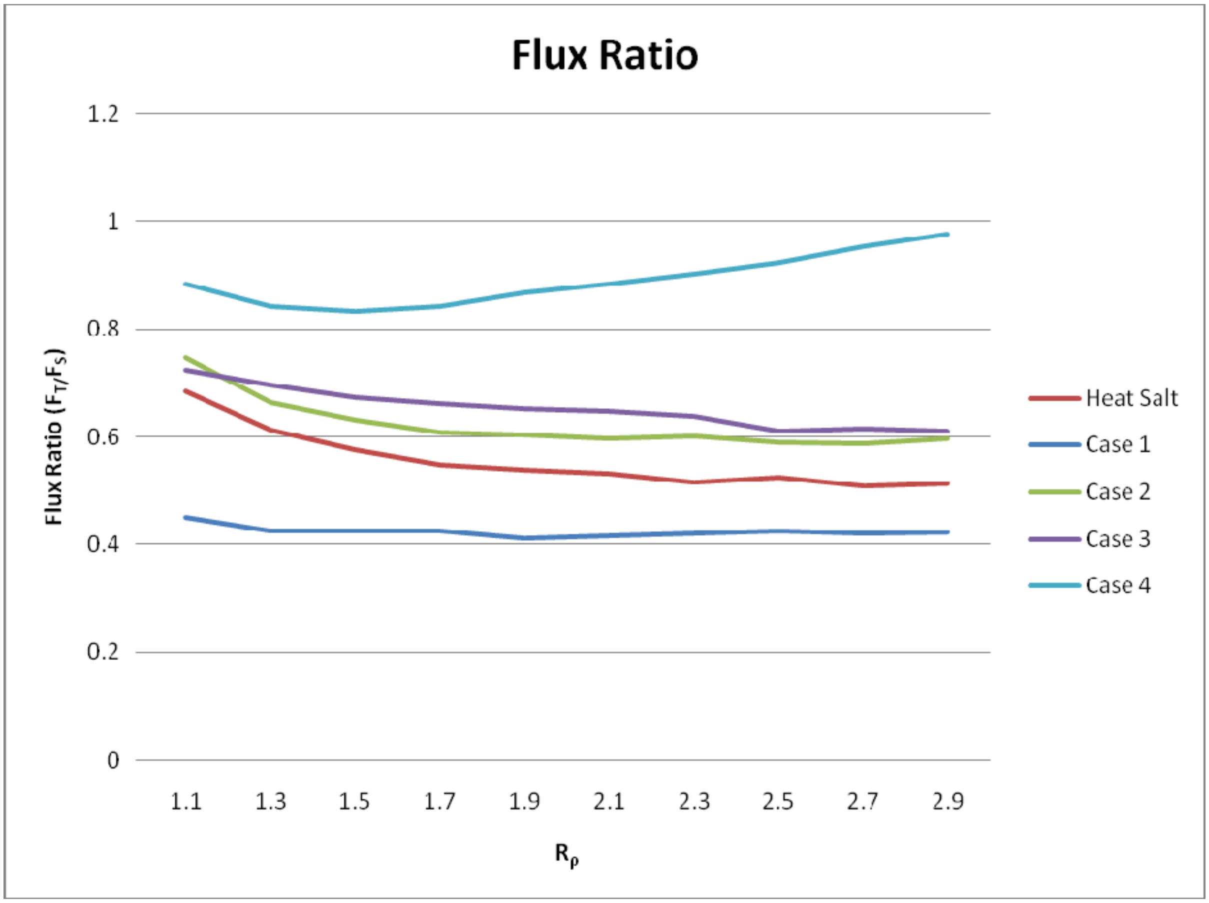

Figure 26. Flux ratio in all case studies.

Another critical parameter, also implicated in the formation of thermohaline staircases, is given by the flux ratio $\left(\gamma = \frac{F_T}{F_S}\right)$. The flux ratio generally decreases with an increase in R_ρ as seen in Figure 26. However, the two cases (3 and 4) with larger diffusivity ratio (τ) show an increase in the flux ratio for higher values of density ratio (R_ρ). Figure 27 and Table 9 represent the flux ratio for each case at a fixed value R_ρ = 1.9, which also indicate that the largest values of flux ratios occur for the largest value of diffusivity ratio.

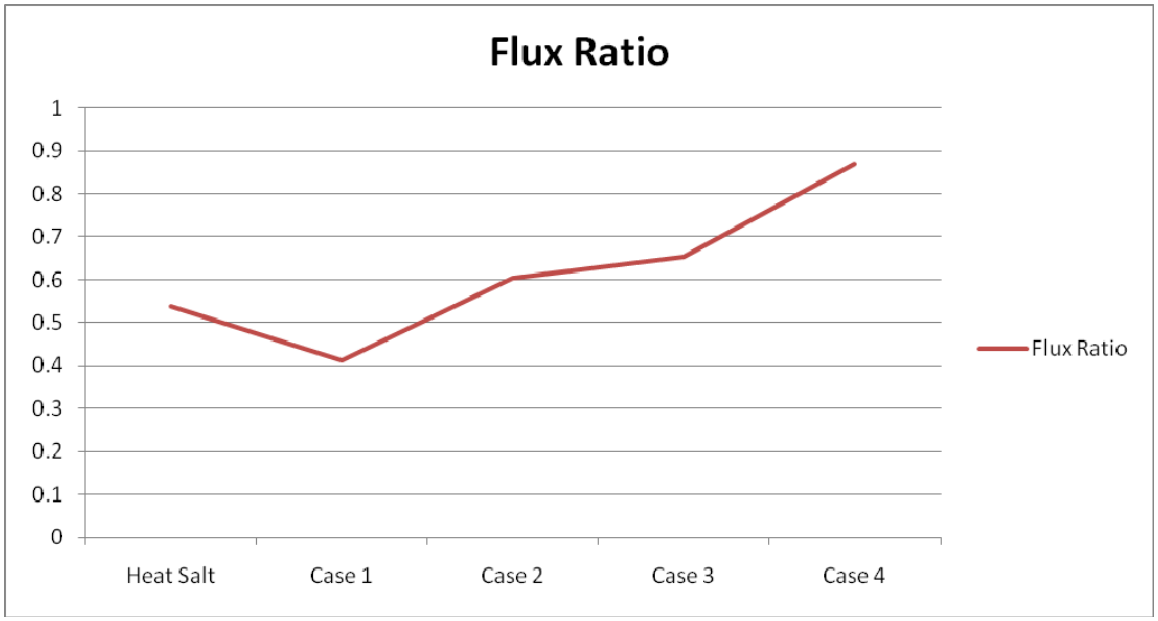

Figure 27. Flux Ratio for all cases at $R_\rho = 1.9$.

Flux Ratio at R_ρ=1.9				
Heat Salt	Case 1	Case 2	Case 3	Case 4
0.538696	0.4116	0.603505	0.65288	0.8690788

Table 9. Flux Ratio for all cases at $R_\rho = 1.9$.

C. COMPARISON WITH THE THEORETICAL MODEL

The relevant values of the adjustable coefficient (*C*) vary only weakly between various cases considered in this study (see Figures 28 through 30). The lowest value of *C*=1.6 (obtained for Case 1) is not too different from that largest value of *C*=2.7 (heat-salt case) considering the range of governing parameters and fluxes. Thus, numerical evidence in this study supports the growth rate balance theory as a conceptual model of the equilibrium salt fingering, capable of predicting dependencies of the equilibrium temperature / salinity transports within a factor of two.

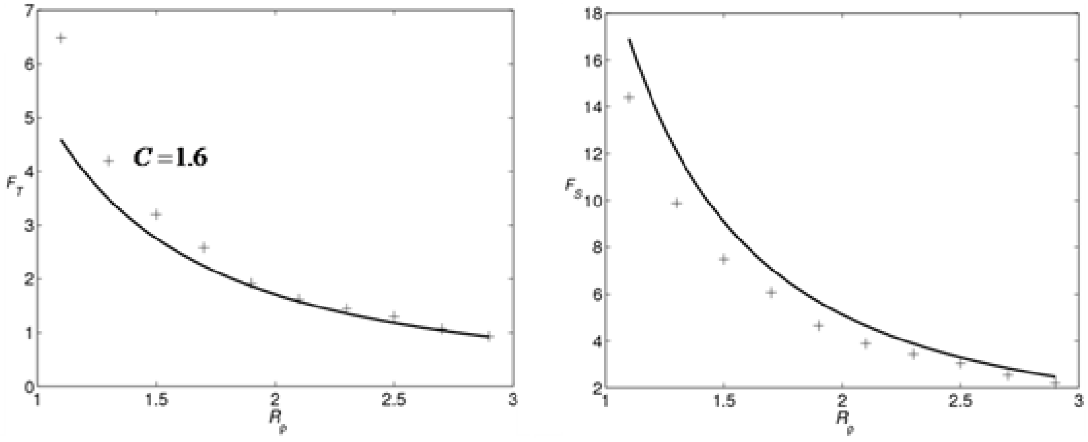

Figure 28. Case 1: Temperature (left panel) and salinity (right panel) fluxes as a function of density ratio (Pr= 0.1, $\tau = 0.01$). Solid curves indicate prediction of the theoretical three-dimensional model and DNS values are represented by plus signs.

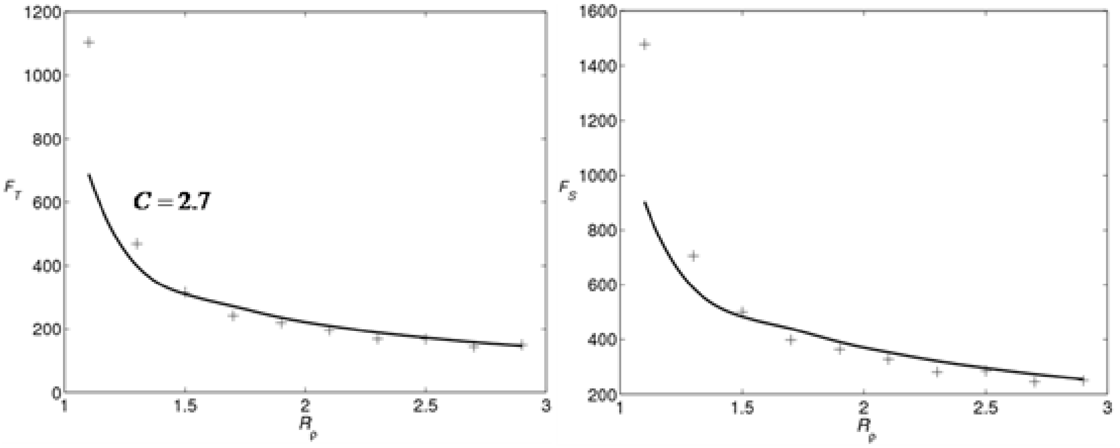

Figure 29. Case 2: Temperature (left panel) and salinity (right panel) fluxes as a function of density ratio (Pr= 100, $\tau = 0.01$). Solid curves indicate prediction of the theoretical three-dimensional model and DNS values are represented by plus signs.

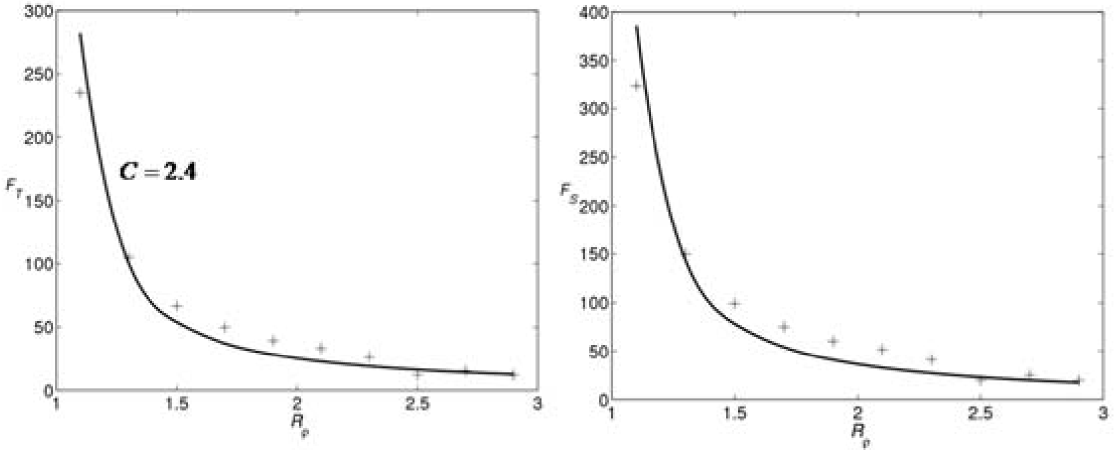

Figure 30. Case 3: Temperature (left panel) and salinity (right panel) fluxes as a function of density ratio (Pr= 7, τ = 0.1). Solid curves indicate prediction of the theoretical three-dimensional model and DNS values are represented by plus signs.

VI. DISCUSSION AND CONCLUSIONS

Double-diffusion is an essential mixing process that may very well drive the larger scale oceanographic circulations and a more thorough study of this phenomenon may lead to higher accuracy in climate and ice melt models and global and regional oceanographic forecast models. Understanding this process requires a series of direct numerical simulations that would not have been possible without parallel processing. The processing time utilized in our study totals over 800,000 hours—350,000 hrs on Department of Defense (DoD) Systems and the remaining on NPS computers. In other words, it would take almost a full century to complete these calculations on a single processor. The parallelization of our de-aliased pseudo-spectral model allowed us to utilize a message passing interface to effectively resolve the complex calculations of fluxes, and therefore derive an understanding of how these micro-scale mixing processes occur in nature. Such an understanding will facilitate our future ability to model these interactions and their effects on large scale circulations. This too requires increased speeds of computer processors in order to process even more data within a timely, forecastable time period.

Our model predicts the following. Double-diffusive transport of heat and salt rapidly intensifies with decreasing density ratio. Fluxes are less sensitive to molecular characteristics, mildly increasing with Prandtl number (Pr) and decreasing with diffusivity ratio (τ). The aspect ratio of individual fingers monotonically increases with Prandtl number, with tall slender fingers realized for large Pr and irregular chaotic fingers for low Pr. Numerically deduced dependency of temperature and salinity fluxes on density ratios are adequately described by empirical Equation (23), with goodness of fit greater than 93% in all calculations. Flux ratio shows an increase at larger R_ρ values for $\tau \geq 0.1$ while constantly decreasing for $\tau = 0.01$.

In addition to the insights based on the numerical modeling, this study presents a phenomenological theory for the vertical transport by salt fingers in unbounded temperature and salinity gradients, which is based on the growth rate balance Equation

(1). By utilizing DNS we were able to plot equilibrium fluxes of temperature and salinity as a function of time and explore their dependency on growth rates. This dependency led us to the discovery of the adjustable coefficient (C) that varies slightly for a wide range of parameters and fluxes. Theory assumes that the statistical equilibrium is reached when the growth rate of salt fingers becomes comparable to the growth rate of their secondary instabilities. This assumption can be rationalized as follows. If the growth rate of primary salt fingers exceeds that of secondary instabilities, then the primary instabilities are unlikely to be affected by perturbations and continue to grow. If, on the other hand, the secondary instabilities grow much faster than fingers, they would rapidly disrupt the primary modes, dramatically reducing their amplitude and transport characteristics. Thus, one is led to a conclusion that the approximate balance between the growth rates of primary and secondary instabilities is inevitable for statistical equilibrium and should be satisfied for a wide range of governing parameters.

It should be understood that the growth rates, both primary (λ_1) and secondary (λ_2), can only be estimated in the order of magnitude sense. Calculation of λ_1 is made for the fastest growing salt fingers – the vertically uniform elevator modes – whereas fully developed double-diffusive convection is generally dominated by irregular structures of finite vertical extent. Similar problems arise for secondary instabilities: λ_2 is estimated for the steady and vertical background field, neither of which is an exact statement. In view of these difficulties, we only claim that the growth rates estimated by our theory should be comparable, but not necessarily equal. Thus, we consider a weak form of the growth rate balance in Equation (1). The nondimensional order one coefficient C in Equation (1) cannot be determined internally on the basis of theory and therefore it was calibrated using direct numerical simulations covering a wide range of governing parameters. For each $(\Pr,\tau)$, theory adequately describes the (rapidly decreasing) dependence of fluxes of diffusing components on density ratio. The calibrated coefficients C are fairly stable. In all three-dimensional simulations – simulations that cover three orders of magnitude in Pr and one order in τ – the values of C are limited to a relatively narrow range $1.6 < C < 2.7$. The theoretical prediction for $C = 2.2$ can explain all the numerical fluxes in this paper within a factor of two. This can be readily rationalized using the growth rate balance Equation (1).

Finally, it is important to emphasize the theoretical significance of our model. We believe that this study opens opportunities for purely analytical explorations that are focused on the growth rate balance Equation (1), rather than on the more complicated original Navier-Stokes system. Our optimism is partially based on the pronounced low-order dynamics of our model. Thus, it is likely that the general character of our solutions could be captured by an analytical low-dimensional model.

THIS PAGE INTENTIONALLY LEFT BLANK

VII. RECOMMENDATIONS FOR FUTURE WORK

Imagine our children and grandchildren planning experiments on Jupiter or other celestial bodies. The work we have done here could play a pivotal role in how they design their sensors and plan their missions. As we have no easy way to achieve direct measurements of these planetary systems, reliable data is often scarce and the spatial location of the elements that need to be measured must be pinpointed to the most scientifically relevant areas. Environmental characteristics of any future planetary system, need to be pinpointed to allow the maximum effectiveness of these future missions.

Even closer to home imagine forecast models, atmospheric and oceanographic, with successful output out to 30 days and beyond. Use of a simple, computationally compact, algorithm for parameterization of micro-scale mixing in general and salt fingers in particular could be implemented in future forecast models would save both processing time and money. Further exploitation of this microscale feature and its impact on large scale circulations can greatly improve climate and operational oceanographic models. Ice melt and climate models could also gain accuracy with the implementation of double diffusive convection. As computer technology improves and processing speeds increase this less computationally taxing algorithm can easily be input into these forecast models.

Successfully modeling double diffusive convection could impact models on magma chamber flows and may even prove vital in volcanic eruptions and possible earthquake predictions. With successful earthquake and volcanic eruption predictions we can also predict tsunamis and have more warning time in order to prepare for these often catastrophic events. The events in the past few years show that these advanced warning systems are needed to prevent the mass loss of life with the “Ring of Fire” surrounding the Pacific Ocean.

THIS PAGE INTENTIONALLY LEFT BLANK

LIST OF REFERENCES

Bagenal, F., Dowling, T. E., McKinnon, W. B., Jupiter: The Planet, Satellites, and Magnetosphere. Cambridge: Cambridge University Press, 2004.

Baines, P. G., and A. E. Gill, 1969: On thermohaline convection with linear gradients. *J. Fluid Mech.* **37**, 289–306.

Balmforth, N. J., and Y.N. Young, 2002: Stratified Kolmogorov flow. *J. Fluid Mech.* **450**, 131–167.

Balmforth, N. J., and Y.N. Young, 2005: Stratified Kolmogorov flow. Part 2. *J. Fluid Mech.* **528**, 23–42.

Balmforth, N. J., S. A. Ghadge, A. Kettapun and S. D. Mandre, 2006: Bounds on double-diffusive convection. *J. Fluid Mech.,* **569**, 29–50.

Canuto, V. M., Y. Cheng and A. M. Howard, 2008: A new model for Double Diffusion + Turbulence. *Geophys. Res. Lett.*, **35**, L02613.

Caplan, S. D. 2008: Microstructure signature of equilibrium double-diffusive convection. Master's thesis, Naval Postgraduate School, Monterey, CA.

Caro, G. P. 2009: Direct numerical simulations of diffusive staircases in the Arctic. Master's thesis, Naval Postgraduate School, Monterey, CA.

Charbonnel, C. and J. Zahn, 2007: Thermohaline mixing: a physical mechanism governing the photospheric composition of low-mass giants. *Astron. Astrophys.*, **467**, L29-L32.

Gargett, A. E., and R. W. Schmitt, 1982: Observations of salt fingers in the central waters of the eastern North Pacific. *J. Geophys. Res., 87*, 8017–8092

Griffiths, R. W., and B. R. Ruddick, 1980: Accurate fluxes across a salt-sugar finger interface deduced from direct density measurements. *J. Fluid Mech.*, **99**, 85–95.

Guillot, T., 1999: Interiors of Giant Planets Inside and Outside the Solar System. *Science*, **286**, 72–77.

Hebert, D., 1988: Estimates of salt-finger fluxes. *Deep-Sea Res.,* **35***,* 1887-1901.

Holyer, J. Y., 1984: The stability of long, steady, two-dimensional salt fingers. *J. Fluid Mech.,* **147**, 169-185.

Howard, L. N., 1961: Note on a paper of John W. Miles. *J. Fluid. Mech.*, **10**, 509−512.

Inoue, R., E. Kunze, L. St. Laurent, R. W. Schmitt, J. M. Toole, 2008: Evaluating salt fingering theories. *J. Mar. Res.*, **66**, 413–440.

Jevons, W. S., 1857: On the cirrous form of cloud. London, *Edinburgh and Dublin Philosophical Magazine and Journal of Science,* 4th Series, 14, 22–35.

Kimura, S., and W. D. Smyth, 2007: Direct numerical simulation of salt sheets and turbulence in a double-diffusive shear layer. *Geophys. Res. Lett.*, **34**, L21610.

Kimura, S. and W.D. Smyth, 2011: Secondary instability of salt sheets. *J. Mar. Res.* (submitted)

Krishnamurti, R., 2003: Double-diffusive transport in laboratory thermohaline staircases. *J. Fluid Mech.,* **483**, 287–314.

Kunze, E., 1987: Limits on growing, finite length salt fingers: a Richardson number constraint. *J. Mar. Res.,* **45***,*533–556.

Lambert, R. B., and Demenkow, J. W., 1972: On the vertical transport due to fingers in double diffusive convection. *J. Fluid Mech.*, **54**, 627–640.

Lick, W., 1964: The instability of a fluid layer with time-dependent heating. *J. Fluid Mech*., **21**, 565–576.

Linden, P. F., 1974: Salt fingers in a steady shear flow. *Geophys. Fluid Dyn*., **6**, 1−27.

Manfroi, A. and W. Young, 1999: Slow evolution of zonal jets on the beta plane. *J. Atmos. Sci.*, **56**, 784−800.

Manfroi, A. and W. Young, 2002: Stability of beta-plane Kolmogorov flow. *Physica D*, **162**, 208−232.

Merryfield, W. J., and M. Grinder, 1999: Salt fingering fluxes from numerical simulations (unpublished manuscript).

Merryfield, W. J., 2000: Origin of thermohaline staircases. *J. of Physical Oceanography*, 30, 1046–1068.

Miles, J. W., 1961: On the stability of heterogeneous shear flows. *J. Fluid. Mech*., **10**, 496−508.

Pickard, G. L., and William J. Emery. Descriptive Physical Oceanography: An Introduction Fifth Enlarged Edition (in SI units). Oxford: Butterworth Heinemann, 1990.

Prikasky, I., 2007: Direct numerical simulations of the oscillatory diffusive convection and assessment of its climatologic impact. Master's thesis, Naval Postgraduate School, Monterey, CA.

Proctor, M. R. E., and Holyer, J. Y., 1986: Planform selection in salt fingers. *J. Fluid Mech*., **168**, 241–253.

Radko, T. and M. E. Stern, 1999: Salt fingers in three dimensions. *J. Mar. Res.,* **57**, 471–502.

Radko, T. and M. E. Stern, 2000: Finite amplitude salt fingers in a vertically bounded layer. *J. Fluid Mech.*, **425**, 133–160.

Radko, T., 2008: The double-diffusive modon. *J. Fluid Mech.*, **609**, 59-85.

Radko, T., 2010: Equilibration of weakly nonlinear salt fingers *J. Fluid Mech.*, **645**, 121-143.

Richardson, L. F., 1920: The supply of energy from and to atmospheric eddies. *Proc. Roy. Soc.* A, **97**, 354−373.

Robinson, J. L., 1976: Theoretical analysis of convective instability of a growing horizontal thermal boundary layer. *Phys. Fluids*, **19**, 778–791.

Schmitt, R. W. 1979: The growth rate of supercritical salt fingers. *Deep-Sea Research,* **26A***,* 23–44.

Schmitt, R. W., 1983: The characteristics of salt fingers in a variety of fluid systems, including stellar interiors, liquid metals, oceans, and magmas. *Phys. Fluids*, **26**, 2373-2377.

Schmitt, R. W., H. Perkins, J. D. Boyd and M. C. Stalcup, 1987: C-SALT: an investigation of the thermohaline staircase in the western tropical North Atlantic. *Deep-Sea Res*., **34**, 1697–1704.

Schmitt, R. W., J. R. Ledwell, E. T. Montgomery, K. L. Polzin, and J. M. Toole, 2005: Enhanced diapycnal mixing by salt fingers in the thermocline of the tropical Atlantic. *Science*, **308**, 685–688.

Shen, C. Y., 1995: Equilibrium salt-fingering convection. *Phys. Fluids*, **7**, 706–717.

Sivashinsky, G., 1985: Weak turbulence in periodic flows. *Physica D*, **17**, 243–255.

Stancliffe, R., E. Glebbeek, R. Izzard, and O. Pols, 2007: Carbon-enhanced metal-poor stars and thermohaline mixing. *Astron. Astrophys.*, **464**, L57–L60.

Stellmach, S., A. Traxler, P. Garaud, N. Brummell and T. Radko, 2011: Dynamics of fingering convection II: The formation of thermohaline staircases. *J. Fluid Mech*., in press.

Stern, M. E., 1960: The “salt-fountain” and thermohaline convection. *Tellus*, **12***,*172–175.

Stern, M. E., 1969: Collective instability of salt fingers. *J. Fluid Mech*., **35**, 209–218.

Stern, M. E., and J. S. Turner, 1969: Salt fingers and convective layers. *Deep-Sea Res.*, **16**, 497–511.

Stern, M. E., T. Radko, and J. Simeonov, 2001: 3D salt fingers in an unbounded thermocline with application to the Central Ocean. *J. Mar. Res.*, **59**, 355–390.

Stern, M. E. and J. Simeonov, 2004: Amplitude equilibration of sugar–salt fingers. *J. Fluid Mech*., **508**, 265–286.

Stern, M. E., and J. Simeonov, 2005: The secondary instability of salt fingers. *J. Fluid Mech.*, **533**, 361–380.

St. Laurent, L., and Schmitt, R. W., 1999: The contribution of salt fingers to vertical mixing in the North Atlantic tracer release experiment. *J. Phys. Oceanogr.,* **29***,* 1404–1424.

Tait, S. and Jaupart, C. 1989: Compositional convection in viscous melts. *Nature*, **338**, 571–574.

Taylor, J. R., and G. Veronis, 1996: Experiments on doubly-diffusive sugar-salt fingers at high stability ratio. *J. Fluid Mech*., **321**, 315–333.

Traxler, A., S. Stellmach, P. Garaud, T. Radko and N. Brummel, 2011: Dynamics of fingering convection I: Small-scale fluxes and large-scale instabilities. *J. Fluid Mech*., in press.

Vauclair, S., 2004: Metallic Fingers and Metallicity Excess in Exoplanets’ Host Stars: The Accretion Hypothesis Revisited. *Astrophys. J.*, **605**, 874–879.

INITIAL DISTRIBUTION LIST

1. Defense Technical Information Center
   Ft. Belvoir, Virginia

2. Dudley Knox Library
   Naval Postgraduate School
   Monterey, California

3. Dr. Jeff Paduan
   Naval Postgraduate School
   Monterey, California

4. Dr. Timour Radko
   Naval Postgraduate School
   Monterey, California